Ragnhild Sæterli

Electronic structure of thermoelectric and ferroelectric materials

- Advanced transmission electron microscopy studies

Doctoral thesis
for the degree of Philosophiae Doctor

Trondheim, July 2010

Norwegian University of Science and Technology
Faculty of Natural Sciences and Technology
Department of Physics

NTNU
Innovation and Creativity

NTNU

Norwegian University of Science and Technology

Doctoral thesis
for the degree of Philosophiae Doctor

Faculty of Natural Sciences and Technology
Department of Physics

ISBN 978-82-471-2285-3 (printed version)
ISBN 978-82-471-2286-3 (electronic version)
ISSN 1503-8181

Doctoral theses at NTNU,

Printed by NTNU-trykk

Preface

This thesis presents some of the work performed during the four-year period from August 2006 to July 2010, which also included one year of teaching duties, as a part of my PhD studies at the TEM group, Department of Physics, Faculty of Natural Sciences, Norwegian University of Science and Technology (NTNU). Some work has, however, been performed at University of Oslo (UiO), Norway, Technical University of Denmark (DTU), and University of Poitiers, France. Supervision has been given by Prof. Randi Holmestad (main supervisor, Department of Physics, NTNU), Prof. Johan Taftø (co-supervisor, Department of Physics, UiO), Knut Marthinsen (co-supervisor, Department of Materials Technology, NTNU) and in part by Antonius T. J. van Helvoort (co-supervisor from 2009, Department of Physics, NTNU). Financial support has been given by The Research Council of Norway, as a part of the project "Studies of the electronic structure of materials at the nanoscale".

Originally, electron energy-loss and convergent beam diffraction experiments on skutterudites were the scope of this PhD. For various reasons, four years down the line the thesis looks quite different, however well within the limitations of the original research project. I am not ashamed to say that many of the projects started out as desperate calls to some of the collaborators, asking if they had any interesting material with some unresolved problems that could be addressed using a TEM and a PhD-student whose latest project turned out to be a dead end. After all, unexpected results are often found in unexpected places, and with that, you also have to accept a certain amount of projects going nowhere but down the drain.

Due to the many and somewhat differing topics of this thesis, I have chosen to divide it into chapters based on the materials in question. Two initial chapters describe the motivation of the studies and gives a general introduction to the main techniques (electron energy-loss near-edge spectroscopy and convergent beam electron diffraction) and relevant material properties (thermoelectricity and ferroelectricity). Subsequent chapters constitute the main part of the thesis, with each chapter comprising an introduction to relevant aspects of the material system, papers and additional work (if any) as well as a short section on conclusive remarks.

An introduction to each paper, including brief descriptions of the paper and my contributions, is given within the chapters. I do, however, for the sake of completeness, list them also here:

Paper 1: Electron energy loss spectroscopy of the $L_{2,3}$ edge of phosphorus skutterudites and electronic structure calculations. Sæterli R, Flage-Larsen E, Prytz Ø, Taftø J, Marthinsen K, Holmestad R. *Phys. Rev. B* **80**, 075109 (2009).

Paper 2: Experimental and theoretical study of electron density and structure factors in $CoSb_3$. Sæterli R, Flage-Larsen E, Friis J, Løvvik OM, Pacaud J, Marthinsen K, Holmestad R. *Accepted for publication in Ultramicroscopy.*

Paper 3: Electronic structure of multiferroic $BiFeO_3$ and related compounds: Electron energy loss spectroscopy and density functional study. Sæterli R, Selbach SM, Ravindran P, Grande T, Holmestad R. *Phys. Rev. B* **82**, 064102 (2010).

Paper 4: Polarization control in ferroelectric $PbTiO_3$ nanorods. Sæterli R, Rørvik PM, You CC, Holmestad R, Tybell T, Grande T, van Helvoort ATJ, Einarsrud M-A. *Submitted to Journal of Applied Physics* (June 2010).

Though I believe there is some useful information in the following pages, I have certainly become wiser during these four years in ways that do not show themselves in scientific papers. Being fond of hiking and mountaineering, I find that these insights have a lot in common to "Fjellvettreglene", guidelines for safe outdoor activities, however read in the light of scientific endeavors. I cite the most relevant of them below, however in Norwegian as I find that my own English translation does not give them the respect that they deserve:

Legg ikke ut på langtur uten trening
Meld fra hvor du går
Lytt til erfarne fjellfolk
Vær rustet mot uvær og kulde selv på korte turer
Gå ikke alene
Vend i tide. Det er ingen skam å snu

Thus, like many other PhD students have learned before me, I too find the final outcome of the years of my PhD study is far from what imagined at the very start. Luckily, perhaps, in some ways. And unfortunately, in others. I regret to say that there is much work put down both from myself and others that for various reasons never found its way to these pages. Likewise, I have had a few detours that have lead to interesting results, but is not a part of this thesis. The outcome of some of them is mentioned below:

Comparison of the electronic structure of a thermoelectric skutterudite before and after adding rattlers: An electron energy loss study. Prytz Ø, Sæterli R, Løvvik OM, Taftø J. *Micron* **39**, 685 (2008).

Molten salt synthesis of plate- and needle-like $K_4Nb_6O_{17}$, $K_2Nb_4O_{11}$ and KNb_3O_8 crystals. Madaro F, Sæterli R, Tolchard J, Einarsrud M-E, Holmestad R, Grande T. *To be submitted.*

Investigations of Bonding in Skutterudites by Electron Energy-Loss Spectroscopy. Prytz Ø, Sæterli R, Holmestad R, Taftø J. Mater. Res. Soc. Symp. Proc. **1044** (2008).

Each of the projects, no matter their outcome, have introduced before me a variety of interesting problems and materials as well as people to collaborate with, each and every one of them bringing me a piece of new insight both scientifically and with regards to "Fjellvettreglene". Thus, the people who deserve to be thanked is quite long, and it is impossible to do them all justice in this way. Let me still mention some of you and the things I appreciate the most, again in Norwegian where I find it appropriate:

Mor, far, Ingvild, Per Erik, Nurket, Ella, Satchmo - Jeg er glad i dere!
Randi - Takk for at du alltid har hatt tro på at jeg skal komme meg gjennom dette, og at du aldri har rynket på nesa når jeg har kommet med et nytt elnes-spekter og ment at det sikkert lå noe å hente her.
Ton - Jeg har alltid satt stor pris på diskusjoner med deg!
Jesper - Takk for all den innsatsen du la ned i CBED-arbeidet! Alltid positiv, alltid hjelpsom.
Knut, Johan, Øystein, Espen, Ole Martin - Det ble ikke gull alt vi tok i, men jammen har vi da fått til litt også! Takk for bra samarbeid i flere runder.
Ravindran - Thanks for all the encouragement and good-will you gave me when approached by a PhD-student you knew nothing about and asked for your data! Most people would probably never even reply to the e-mail, you did - and I believe we made a great paper.
Jerome, Takeshi - Thank you both for your great hospitality and helpfulness

on my visits.
Sverre, Per Martin, Fransesco, Tor, Mari-Ann - Dere vet det godt, men jeg sier det likevel: Uten at jeg hadde fått lov til å hente med meg restene fra labforsøkene deres for å putte det i TEM-en hadde det ikke vært noen avhandling på meg.
Bjørn - Unnskyld for alle de sene kveldene og helgene jeg har ringt for å fortelle at noe er feil på mikroskopet. Din tålmodighet er tilsynelatende uendelig!
Malin, Åsmund, Magne, Espen, Erik, Marius og resten - Uten lunsjene deres kunne dette fort blitt fire triste år. Dessuten, hvem sa at store ideer bare kommer når du sitter på kontoret?

And now, with the clichés over and done with, and with no further ado, here it is: My thesis. Enjoy!

Summary

This thesis describes TEM studies related to the electronic structure of thermoelectric and ferroelectric materials.

Compounds within the thermoelectric skutterudite class of materials were examined using Electron Energy-Loss Near Edge Spectroscopy (ELNES) and Convergent Beam Electron Diffraction (CBED) in order to shed light on bonding mechanisms. Using ELNES in combination with two different theoretical calculation schemes (density functional theory (DFT) and real-space multiple scattering (RSMS) calculations) on various Phosphorus-containing skutterudites, it was shown that the compounds are remarkably similar in their Phosphorus bonding environment and the experimental results are well described by both theoretical approaches.

CBED measurements on the skutterudite $CoSb_3$ yielded two refined structure factors that were compared to and could serve as a reference to DFT calculations and X-ray diffraction experiments on structure factors.

ELNES experiments on the ferroelectric $BiFeO_3$ and two isostructural cation substituted compounds have been compared to DFT and RSMS calculations to obtain insight into the electronic structure of these compounds and the role of the two different cations. These were found to be interrelated through small, but finite covalent bonds to oxygen.

$PbTiO_3$ nanorods were examined by conventional TEM techniques to reveal the ferroelectric domain structure. Microtomed slices of the nanorods provided insight into the surfaces and internal defects in the nanorods. Further experiments on the nanorods using holography to attempt to image the domain structure as well as a scanning transmission electron microscopy and a high resolution approach to image strain are described.

Finally, preliminary ELNES experiments on the ferroelectric $HoMnO_3$ are reported.

Contents

Chapter 1

Motivation

As I see it, there is a two-fold reason behind the scientific quest of unveiling the truth about the world in which we are living. Firstly, mankind is curious by nature - we want to know what lies beyond the seas or mountain ranges, we want to know what the dark side of the moon and the inside of the earth look like, we want to know what happens if we do this, and why, and how! Secondly, we want to make this world a better place to live for ourselves and those around us. Without going into details, much can be said about the success of his aim, about nuclear power and atomic bombs, antibiotics and resistant bacteria, increasing standards of living and disturbing the natural balance of the earth. Still, I believe these two driving forces are present in all great scientists, and also (without considering further similarities) in me. And I sincerely believe in the fruitfulness also of the former, as great discoveries have proven hard to plan and usually pop up in the most unexpected of places. A wise man or woman once said that the most ground-shaking scientific discoveries are not preceded by a ”Wow!”, but rater by a ”Hmm... That’s funny.”

This is also reflected in the topic of this thesis, trying to combine a scientific curiousness with making a difference. The study of materials at the nanoscale still offers a broad range of challenges in terms of properties and phenomena not yet understood, while on the same time carries great potential for solving some of today’s most important global challenges.

This study will focus upon two classes of materials, thermoelectric and ferroelectric materials, and try to shed some light on the electronic properties of those. Thermoelectric materials are conductors or semiconductors that will respond to a temperature difference by setting up an internal electrical field that can be used to run currents through a circuit, and oppositely, if exposed to currents, can make a temperature difference. Either of these usages carry a promise to decrease energy usage or pollution, the former by converting (waste) heat to usable energy and the latter by refrigeration without harmful gases or liquids [1]. Although used already today in various niche markets such as powering space crafts [2], medical devices [3, 4] and refrigerators where usual methods are not convenient [5], the efficiency of thermoelectric materials are still low (5-12%, depending on usage) [6]. Attempts to increase this efficiency include nanostructuring of materials [7] and tailoring of properties [8] - both methods relying heavily on understanding the electronic structure of these materials, as it influences the two parameters most vital to the thermoelectric efficiency: Their ability to carry heat and to conduct electrons.

The second class of materials that this thesis comprises, ferroelectric materials or simply ferroelectrics, is materials which exhibit a switchable internal electric field (polarization) even in the absence of an external field. The ability to control the direction of this polarization into one out of to two (or more) possible states, is the background of the usage of ferroelectric materials in ferroelectric memory devices (FeRAM) already on the market [9]. Other applications of ferroelectrics rely not on the ferroelectric properties themselves, but rather other properties always present in a ferroelectric such as piezoelectricity (a coupling between strain/stress and polarization), pyroelectricity (a coupling between temperature and polarization) or a high dielectric constant. These properties make ferroelectrics useful in a variety of devices ranging from sound generation and detection systems to infra red (heat detection) cameras and step motors controllable down to the nanoscale [10, 11]. There is not a single microscopic origin of polarization for all ferroelectric materials. Rather, there is a multitude of reasons for ferroelectricity which all have in common that for some reason, the positive charges (atom cores) in the material are slightly misaligned with the negative charges (the electrons). Thus, in the pursuit of ferroelectric materials with specific properties, the electronic structure plays an important part.

As always, if you want to improve a property of a material, there are two ways of proceeding: You can go ahead making and examining all sorts of compounds hoping that the perfect thing will pop up, or you can sit down and try to figure out what makes the material carry the property you are after. Me, I prefer the latter. So here is the point I am trying to make: The first step in this will always have to be to understand what you have already. And cross your fingers that the right ”Hmm... That’s funny” will come along. The aim of this study has therefore been to fill in some small, but hopefully relevant gaps that have been present in our understanding of the electronic structure of certain ferroelectric and thermoelectric materials.

And in the subject of properties of materials, how they behave, the electronic structure is decisive in more than one way. The energies and behavior of the tiny electrons circling (or whirling or jumping or whatever it is electrons do) around the atom core determines chemical, optical, electrical, magnetic, and even thermal properties of the material in which they reside. It is therefore no wonder that tons of books have been written and years and years of research has been put into the field of electronic properties of materials. And still, there is much left to understand, from the most intricate theoretical understanding of electron behavior - the most used simplification in the field is, still today, that the electrons in a material are unaware of each other, a simplification that is obviously not correct but that simplifies the picture enormously - to how to make the electrons behave the way we want them to in for example micro (and nano!) electronics. It is perhaps not surprising, then, considering the vast opportunities that electrons offer us, that the main instrument that I have chosen to use in the study of these materials, is based on - exactly! - electrons.

References

[1] Di Salvo FJ: *Thermoelectric cooling and power generation.* Science **285**, 703 (1999).

[2] *NASA Fact Sheet: Spacecraft Power for Cassini* (1999). `http://saturn.jpl.nasa.gov/multimedia/products/pdfs/power.pdf`. Downloaded 20.05.2010.

[3] Yang Y, Wei XJ and Liu J: *Suitability of a thermoelectric power generator for implantable medical electronic devices.* J. Phys. D: Appl. Phys. **40**, 5790 (2007).

[4] Xie J, Lee C and Feng HH: *Design, Fabrication, and Characterization of CMOS MEMS-Based Thermoelectric Power Generators* J Microelectromechanical Syst, **19**, 317 (2010).

[5] Sales BC: *Smaller is cooler.* Science **295**, 1248 (2002).

[6] Bell LE: *Cooling, heating, generating power, and recovering waste heat with thermoelectric systems.* Science **321**, 1457 (2008).

[7] Dresselhaus MS, Chen G, Tang MY *et al.*: *New directions for low-dimensional thermoelectric materials.* Adv. Mater **19**, 1043 (2007).

[8] Chen G, Dresselhaus MS, Dresselhaus G, Fleurial JP and Caillat T: *Recent developments in thermoelectric materials.* Int. Mater. Reviews **48**, 45 (2003).

[9] Scott JF: *Applications of modern ferroelectrics.* Science **315**, 954 (2007).

[10] Rabe KM, Ahn CH and Triscone J-M: *Physics of ferroelectrics: a modern perspective.* Springer-Verlag Berlin Heidelberg (2007).

[11] Muralt P: *Ferroelectric thin films for micro-sensors and actuators: a review* J. micromech. microeng. **10**, 136 (2000).

Chapter 2

General background

2.1 Probing the electronic structure of materials

2.1.1 Bands and bonds

Pauli's exclusion principle tells us that as atoms are brought closer and closer together, the allowed energy values of their electrons take on the shape of energy bands rather than discrete values. In a crystal, these energy bands vary throughout the unit cell. It is the properties of these energy bands that separate insulators from metals, and that determine excitation properties of the material such as color (see any standard solid state physics book, such as e. g. [1]).

A closely related concept is that of bonds, which is what holds the atoms in the material together. They form as the atoms are brought close together and are a result of a lowering of the total energy of the atoms compared to free atoms. There are several such types of bonds, of which the most important to this thesis are covalent and ionic bonds. Common to all of them is that they influence the electron density of the material; the ionic bond by transferring charge between atoms, and the covalent bond by directing electrons to certain areas in space (and thereby depleting others) [1]. As we will see examples of throughout this thesis, most materials have bonds that cannot be classified as purely one or the other. Also, bonding and the way electrons interact with each other (electron correlation effects) determine most material properties and can lead to exotic phenomena such as ferromagnetism, ferroelectricity and superconductivity.

Information on bonding arrangements can be obtained through examination of the *spatial arrangement* of electrons in the material, as both types of bonds introduce a charge redistribution. The *energies* of the electrons and their bands offer another point of view on the same phenomenon, as bonding will inevitably alter the electron energies and band structure. Two experimental techniques emerging from these different angles on bonding will be the topics of the next sections, starting with an energy probing technique.

2.1.2 Electron energy-loss near-edge spectroscopy

Electron Energy-Loss Spectroscopy (EELS) comprises several techniques usually performed within a transmission electron microscope (TEM). As no general TEM theory will be given here, the reader is referred to introductory books such as that of Williams and Carter [2], which gives an easily comprehensible and still quite thorough introduction to any subject related to TEM. For more specific and advanced EELS theory, the book by Egerton [3] is a comprehensive review of underlying physics and also applications.

The EELS techniques are capable of revealing information on the sample as diversified as composition, recently also on an atomic scale [4], bonding and valence [5, 6], thickness [7], optical [8] and even mechanical properties [9]. The major advantage of using EELS compared to the related X-ray absorption spectroscopy techniques, is first and foremost the unique capability of combining energy-loss experiments with imaging, diffraction and other techniques in the same instrument and session, down to atomic resolution.

The EELS techniques have in common that they exploit the energy loss of a nearly monochromatic (to within $10^{-4}\%$) beam of electrons as it passes through a thin (usually a few tenths of nanometers) sample. The electrons in the beam can interact with the sample in a number of ways, some relevant ones are being depicted in figure 2.1 together with their approximate scattering angle θ.

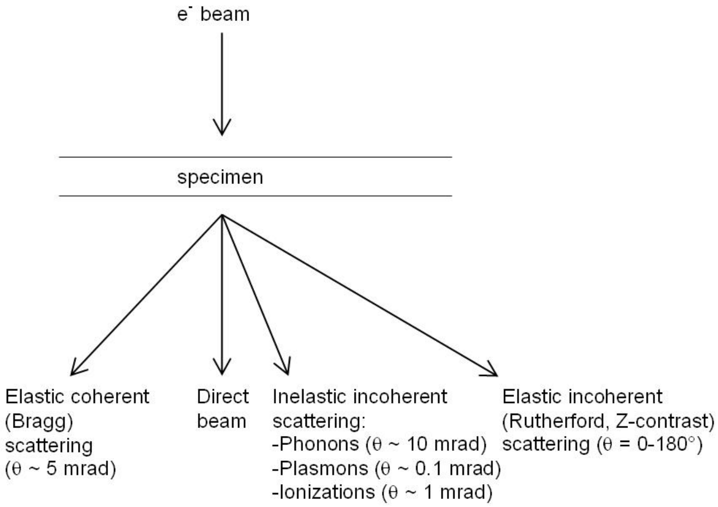

Figure 2.1: *Some relevant signals due to high-energy electron interaction with a thin specimen in and their scattering angle θ.*

Roughly, the signals can be divided into the two categories *elastic* and *inelastic* scattering depending on their origin. Elastic scattering involves an interaction with the nucleus of the atom which, by virtue of its enormous mass compared to that of the electron, causes a very small (usually immeasurable) energy loss[1]. In a crystal, this elastic scattering (now called diffraction) is confined to certain angles, the Bragg angles. Also the excitation of phonons, collective vibrations of the atomic lattice, is, in the language of TEM-EELS, considered elastic as the associated energy loss in the order of meV is too small to be detected. Though not directly applied in EELS, elastic scattering can, through multiple scattering events, modify the angular range of the inelastic scattering or spatial location of the electron beam with respect to the atom cores [3].

Another useful distinction is between *coherent* and *incoherent* scattering; in the former case there is a relationship between the phases of the scattered electrons while in the latter these are uncorrelated. Loosely speaking, inelastic scattering can be treated incoherently while elastic scattering is more coherent, the exception being high-angle elastically scattered electrons [2].

The relevant inelastic scattering processes are due to interactions with the electrons in the sample. Outer (more weakly bound) electrons give rise to collective plasmon excitations, while single-electron excitations give rise to ionization edges in the spectrum. A typical EELS spectrum (from $BiFeO_3$) is shown in figure 2.2. Note the change in scale at an energy loss of about 450 eV, emphasizing the intensity difference between the low-loss region (up to ~ 50 eV) and the higher energy loss area. The low-loss area contains the Bragg scattered, phonon scattered and unscattered electrons in the so-called zero-loss peak, which for usable sample thicknesses is the most intense feature of the spectrum. Further, electrons scattered by plasmons are found in the region around an energy loss of a few tenths of eV. Further up in energy loss are the core edges (the O K and Fe $L_{2,3}$ edges are marked in 2.2) superimposed on an approximately exponentially decaying background[2].

What will be the focus here is Electron Energy-Loss Near Edge Structure (ELNES) [6, 10], a technique employing core-losses to extract information on the local electronic structure of a material. The perhaps easiest application is phase identification or "fingerprinting" [11], as the near-edge shape varies according to local atomic environment and bonding. The so-called white line intensity of the transition metal L edges [12, 13] and the related valency measurements [14, 15] are other well-known examples.

---

[1] The exception being backscattered electrons, electrons that are scattered to very large angles, which can lead to energy losses of several eV. Due to their large scattering angles, these are not measured in EELS.

[2] Resulting mainly from tails of preceding core edges, valence electron scattering and multiple scattering events (usually a combination of core and plasmon scattering) [3].

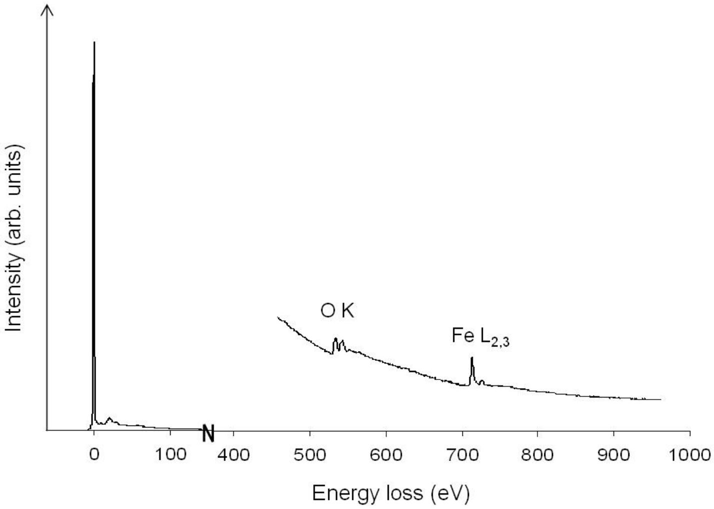

Figure 2.2: *An example of an EELS spectrum from BiFeO*$_3$*. The O K and Fe* $L_{2,3}$ *edges at approximately 530 and 720 eV are marked. The energy loss axis is cut at 150 eV and there is a change in the intensity scale at 450 eV to account for the lower intensity of the core edges compared to the low-loss area.*

The core losses emanate from beam electrons that have lost energy to excite a single inner-shell (core) electron up to the conduction band, giving it a final energy $E_f \geq E_F$, E_F being the Fermi energy. This is illustrated schematically in figure 2.3. While we will soon analyze the probability for an electron to have a certain energy loss, the overall trend is a decreasing probability for higher energy, which is what gives the core losses their edge shape and name. The edges are further named after the initial state of the core electron, with the quantum number n being expressed by a letter starting with K and running alphabetically for higher values of n. Further, a numerical subscript indicates the value of the quantum numbers l and j, as indicated in figure 2.3.

During a core electron interaction, the high energy beam electron is scattered to a typical angle of a few mrads [16], transferring the momentum q and energy $E = E_f - E_i$ (usually 100-1000 eV in the core excitations typically used in ELNES measurements) to excite the core electron from an initial state $\mid \Psi_i\rangle$ to a final state $\mid \Psi_f\rangle$. In the one-electron approximation,

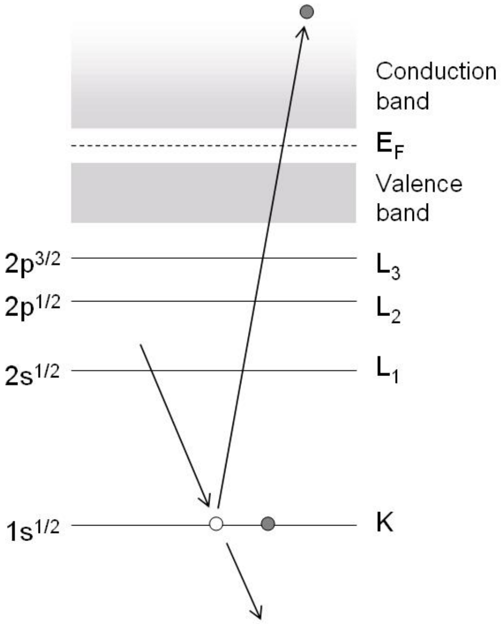

Figure 2.3: *Schematic drawing of a core excitation and the corresponding nomenclature.*

the probability for such an excitation process is

$$\frac{d^2\sigma}{d\Omega dE} \propto \frac{\gamma^2}{a_0^2 q^4} \mid \langle \Psi_f \mid \exp\left(i\mathbf{q}\cdot\mathbf{r}\right) \mid \Psi_i\rangle \mid^2 D(E) \tag{2.1}$$

where a_0 is the Bohr radius, γ is the relativistic correction factor and $D(E)$ is the density of states (DOS). The one-electron approximation describes the process as influencing the excited core electron alone, leaving the rest of the atomic electrons in their ground state. While this is a useful first approximation, the excited electron leaves behind a core hole that to a certain degree modifies the energies of the other electrons of the excited atom and thus the potential distribution[3]. Hence, the final state $\mid \Psi_f\rangle$ is not strictly a ground state, but rather a state of the excited atom.

---

[3] A rule of thumb has been that metals, with free electrons, are more likely to screen the core hole than semiconductors and especially insulators, so that the effect of the core hole should be less in metals. There are, however, several reports that taken together leads to the conclusion that the effect of the core hole is more complex and relying on other factors such as which edge is probed (see e.g. [17, 18, 19].

To simplify the situation further, we will introduce a few more useful approximations. First, the dipole approximation assuming a small momentum transfer is usually applied so that the $\exp(i\mathbf{q}\cdot\mathbf{r})$ term is Taylor expanded and only the term $\mathbf{q}\cdot\mathbf{r}$ is left. Only transitions with a change in angular momentum $\Delta l \pm 1$ are thus considered. Experimentally, this is achieved by using an aperture in the reciprocal space to limit the angular range of electrons contributing to the energy-loss spectrum. The remaining term $\mid \langle\Psi_f \mid \mathbf{q}\cdot\mathbf{r} \mid \Psi_i\rangle \mid^2$ is usually called the matrix element, and dictates the spatial overlap of the initial and final states.

Second, the initial state is in ELNES usually considered purely atomic and sharp so that the DOS correspond to that of the final state[4].

With the spatial overlap being negligible between states localized on different atoms and due to the validity of the dipole approximation, the shape of the core edge is thus a representation of the site- and symmetry projected unoccupied DOS.

Experimentally, the perhaps most critical issue is the sample thickness t, usually described in units of mean free path of scattering (λ). As multiple scattering becomes important already at a low (<1) t/λ value, it is usually not recommended to work with samples thicker than a few tenths of nanometers. This also calls for care when preparing specimens, as any top - and bottom amorphous layer has to be minimized. While the orientation of the sample could influence the spectrum immensely and a lot of useful information can be extracted from such orientation-dependent experiments [20, 21, 22], strong channelling conditions are usually avoided in regular ELNES experiments [23] and often a sum over several (non-channelling) orientations is employed.

Further, the angular dependence of scattering needs to be considered. The use of an angle-limiting aperture to prevent non-dipole transitions has already been discussed. As the background scattering processes are generally scattered to higher angles, the use of such an aperture will also increase the signal to background ratio. The cost of this is a decrease in the signal to noise ratio, so that a compromise has to be employed. Usually, a value around 2-3 times the characteristic scattering angle $\theta_c \approx E/2E_0$, is recommended, E being the energy loss in question and E_0 the beam energy. For energy losses of some hundred eV and a beam energy of 200 keV, this amounts to an aperture size in the order of a few mrads. [3].

---

[4] At lower energy losses this is not valid anymore, and a convolution between initial and final DOS has to be considered [3].

2.1.3 Electronic structure and energy-loss calculations

Though a wealth of information on the local electronic structure of a material is potentially available through the energy-loss spectrum, ELNES is a technique which for a long time has been held back by a lack of ways of interpreting the data. The ability to interpret and understand the more complex features of the spectra is dependent on models and theoretical approaches. With the rise of density functional theory (DFT), comparison to fairly accurate (although mostly ground state) DOS calculations have become possible [24]. From the related field of X-ray absorption near-edge structure measurements other calculation schemes such as FEFF [25] has risen, being able to simulate experimental spectra and predict also excited properties. Thus, simulations and interpretation of experimental data has become more and more widespread and has been determining in ELNES finding its way into the standard material characterization toolbox.

For several of the materials studied here, the real-space multiple scattering (RSMS) program FEFF [25] has been applied to interpret the near-edge fine structure. Although formally equivalent to reciprocal space formulations such as various DFT approaches [26], FEFF calculates the various scattering paths in a specified cluster of atoms in real space. Realistic clusters consist of a few hundred atoms, usually enough to ensure convergence of the data. Later versions include self-consistent fields and relativistic effects [27], with a spherical muffin-tin potential. FEFF is also able to generate DOS of the cluster, however broadened due to finite size-effects. Not being a ground state calculation scheme, FEFF can incorporate excitation effects like core holes and non-periodic effects like boundaries and defects, while effects due to electron correlation and magnetism are not yet addressed [26].

2.1.4 Convergent beam electron diffraction

While the EELS techniques are concerned with inelastic scattering and the energies of the electrons, also the elastically scattered electrons can yield information on bonding. Of TEM techniques utilizing elastic signals, Convergent Beam Electron Diffraction (CBED) is a powerful technique for analyzing a wide range of material properties, from fairly simple thickness measurements [28] to complex symmetry and space group assignments [29], lattice parameter determination [30], defects [31] and electronic structure determination [32].

One of the main advantages of using electron diffraction rather than X-ray or neutron diffraction, is the ability to focus the probe down to Ångstrøm size. This is vital in the study of nanostructures and phenomena at the nanoscale, but also makes the study of defect-free areas of a crystal feasible as suitable areas can easily be found by setting the TEM to image mode. Another aspect of using electrons is the need for dynamical theory, as the mean free path of scattering under normal CBED conditions is substantially less than the sample thickness [33]. This certainly complicates interpretation of the patterns, but can on the other hand be used to extract the phases of the structure factors without the phase and extinction problems of X-ray diffraction [28].

Determinations of structure factors from CBED and X-ray diffraction are in many ways complementary to each other[5], as X-ray diffraction excels at determining many high-order structure factors while CBED is useful for determining a few of the low-order ones [28]. These low-order structure factors are not to be overlooked, as they contain information on the charge density in the area between the atomic cores and thus valence electron density and bonding.

An introduction to electron diffraction theory can be found in any standard TEM book such as Williams and Carter [2], while a more in-depth review is given by Humphreys [33] and is recommended to the interested reader. While the basic theory of CBED is the same as that of selected area (parallel beam) diffraction, a complete overview of electron diffraction theory which focuses on CBED is given by Spence and Zuo [28]. Here, only a brief overview of the topic is given, with emphasis on parameters and considerations important for this thesis.

In CBED, the (almost) parallel beam of conventional TEM is replaced by a convergent beam with a semiangle of usually a few mrads, so that the spot pattern observed in selected area diffraction is broadened into disks, see figure 2.4 for the scattering geometry and an example CBED pattern from $CoSb_3$. For non-overlapping disks, the intensity in each point in the disk reflects the scattering conditions of a certain incidence angle (or equivalently, crystal orientation), so that the CBED pattern corresponds to a series of rocking curve measurements, all taken from the same area of the crystal.

---

[5] Though electron and X-ray structure factors do not measure the same quantity: While the X-ray structure factor measures the Fourier transform of the electronic charge distribution, the electron structure factor also includes contributions from the nuclear core. However, by knowledge of the atomic positions and the temperature factors, a conversion and thus comparison between the X-ray and electron structure factors is possible.

The use of a coherent electron source modifies this picture in the case of overlapping disks, so that these areas are unsuited for quantitative work [34].

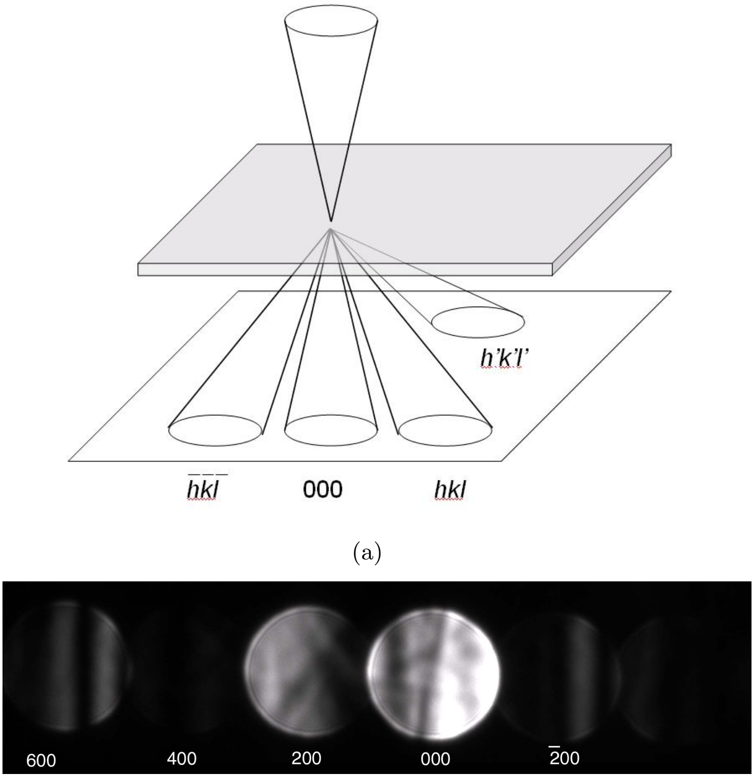

(a)

(b)

Figure 2.4: *(a) Schematic CBED geometry showing four excited beams, three of which lies on a systematic row. (b) Experimental CBED image of* $CoSb_3$ *systematic row (00 2n disks).*

The dynamical intensity in each point in a disk is a complicated function of sample thickness, orientation and structure factors. In quantitative CBED, this intensity is usually derived using Bloch wave theory. The basic idea of Bloch wave theory is that the wave function of the beam electrons inside the (crystalline) sample can be expressed as a linear combination of plane waves, the so-called Bloch waves. The Bloch waves have the periodicity of the crystal, but their magnitudes vary across the unit cell and depth of the crystal. The intensity of a point in disk **g** specified by an incident beam wave vector $\mathbf{K}$ in a sample of thickness t is given as

$$I_{\mathbf{g}}(\mathbf{K}) = \left| \sum_j C_0^j C_{\mathbf{g}}^{j*} e^{2\pi i \gamma^j t} \right|^2 , \tag{2.2}$$

where the Bloch wave coefficient $C_{\mathbf{g}}^j$ and anpassung γ^j of the j'th Bloch wave are found by diagonalization of the time-independent Schrödinger equation for an independent electron in a periodic potential field[6], see e.g. [28].

In principle, there are equally many Bloch waves as there are diffracted beams. As each diffracted beam depends on all of the Bloch waves and vice versa, an exact solution can only be found by considering an infinite number of beams. Since longer computing times are needed as the number of included beams increases, in practice only the strongest beams are used in the calculations. The selection of strong beams is based on criteria such as reciprocal lattice vector, closeness to the Ewald sphere and strength of the structure factor [35]. The effect of additional, weaker beams can be incorporated by Bethe perturbation theory [28].

In practice, determination of structure factors is accomplished by careful matching between experimental intensity values and simulated ones. Though both systematic row orientations as that shown in figure 2.4(b) and zone-axis patterns can be used, the advantage of several available structure factors of the latter has to be weighed against the disadvantage of having to include more beams into the calculations. To further reduce computation time, the intensity is usually measured and simulated in only a segment of the disks, for example in one or more linescans across the disks. Done in a loop, this refinement of parameters does not only include the desired structure factor, but also experimental parameters such as beam direction, sample thickness and background intensity.

Careful control of other experimental parameters such as various camera characteristics [36], sample temperature and beam convergence and energy is also vital to obtain a correct structure factor, along with knowledge of material characteristics such as lattice parameters and atomic displacement factors [37].

---

[6] By neglecting of electron spin as well as exchange and correlation effects and introduction of proper boundary conditions.

2.2 Thermoelectricity

A thermoelectric material is, simply speaking, a conductor or semiconductor which is able to turn a temperature difference into an electric voltage or vice versa. Traditionally, the thermoelectric effect is divided into three related linear effects; namely the Seebeck, Peltier and Thompson effects. These thermoelectric phenomena are most easily understood by realizing that electronic current carriers, electrons and holes, also are carriers of heat. Thus, a coupling between charge and heat currents is achieved in materials with free charge carriers. Here, a hand-waving classical explanation of the thermoelectric effects is given before evaluating some of the important parameters that determine the thermoelectric response of a material. A more thorough description can be found in e. g. [38].

2.2.1 Theory of thermoelectricity

The Seebeck effect states that upon applying a temperature difference $\mathrm{d}T$ to a material containing free charge carriers, a voltage difference $\mathrm{d}V$ is achieved. The response of the material, the Seebeck coefficient or thermopower S, is phenomenologically given as the ratio of this voltage difference and the temperature difference, $S = dV/dT$. Microscopically, the effect can be explained by considering a slab of material with a temperature difference between the two ends. The charge carriers[7] at the hotter end carry more thermal energy than the charge carriers at the colder end. This thermal energy makes the diffusion of charge carriers faster, so that the hot charge carriers travel faster to the cold side of the material than the cold charge carriers move to the hot side. The result is a charge accumulation (negative or positive depending on the sign of the charge carriers) on the cold side of the material, which in turn creates an electric field along the direction of the temperature gradient so that eventually an equilibrium situation occurs where the diffusion due to the temperature difference is exactly opposed by electric field. This is illustrated in figure 2.5. Upon connecting the material to an external electrical circuit, this charge accumulation can be avoided and the excess charges will instead manifest themselves as a current through the circuit.

---

[7] Electrons and/or holes. If both are present in the material, they carry heat in opposite directions, thereby reducing the effect. Usually, therefore, doped semiconductors are preferred.

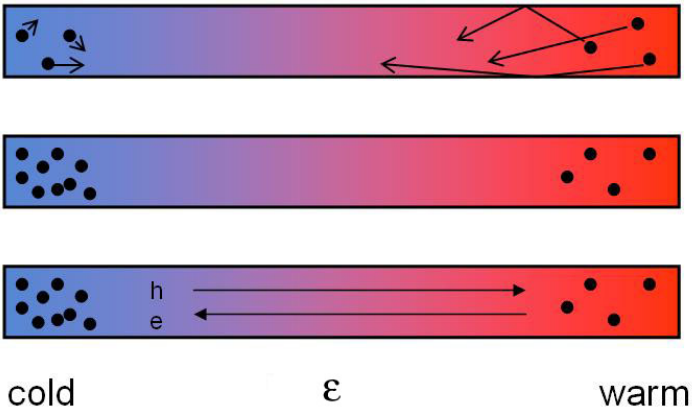

Figure 2.5: *Illustration of the Seebeck effect. Top: Charge carriers at the hot end of the material diffuse faster than charge carriers on the cold side, creating charge accumulation on the warm and cold side (middle). Bottom: Equilibrium situation where charge accumulation is balanced by the resulting electric field ε, the direction depending if the charge carriers are electrons (e) or holes (h).*

The Peltier effect is the effect that upon connecting two materials with different Seebeck coefficients, any current sent through the system will release or absorb heat at the junction. This is explained by considering that the current density must be equal on both sides of the junction. If then the materials on each side of the junction have differing Peltier coefficients, that is, the charge carriers in the two materials do not carry the same amount of heat, the heat absorption has a discontinuity at the interface resulting in a release or absorption of heat at the interface. The Peltier effect can be described by a Peltier coefficient Π relating the heat absorption per time unit, w, to the current I through the relation $w = \Pi I$. The Seebeck and Peltier coefficients are related by the Thompson equation $\Pi = ST$, T being the absolute temperature of the material.

There is also a third thermoelectric effect, the Thompson effect, which comes into play when both an electric field and a temperature gradient are present in a material. It can be understood by realizing that the material response to a temperature difference, the Seebeck coefficient S, might itself depend upon temperature. Thus, if a temperature gradient exists along with a current and the Seebeck coefficient varies in magnitude within the material, the situation is analogue to how the Peltier effect creates a release or absorption of heat at an interface of materials with different Π (and $S = \Pi/T$). Hence, due to a gradual rather than sharp change in the Seebeck coefficient, heat is released or absorbed in the bulk of the material according to $Q = -\beta j dT/dx$, j being the current density and dT/dx the temperature gradient along the current direction in the material. β, the Thompson coefficient, is related to the Seebeck coefficient by $\beta = T dS/dT$.

A commonly used measure of the efficiency of thermoelectric properties is the thermoelectric (dimensionless) figure of merit zT, defined as

$$zT = \frac{S^2\sigma}{\lambda} T \tag{2.3}$$

where σ is the electrical conductivity and λ the thermal conductivity of the material. This emphasizes that a high Seebeck coefficient is necessary for the thermoelectric performance, as well as a high electrical conductivity (to keep the voltage difference high) and low thermal conductivity to ensure that the temperature difference in the material is not easily evened out by heat leakage from the hot to the cold side.

In mathematical terms, the expression for the Seebeck coefficient reads [39]

$$S = \frac{1}{eT} \frac{\int_0^\infty \sigma(E)(E - E_F)\frac{\mathrm{d}f_0}{\mathrm{d}E}\mathrm{d}E}{\int_0^\infty \sigma(E)\frac{\mathrm{d}f_0}{\mathrm{d}E}\mathrm{d}E}. \tag{2.4}$$

Here, E_F is the Fermi energy[8] and f_0 is the Fermi-Dirac distribution. As $\mathrm{d}f_0/\mathrm{d}E$ is symmetric about the Fermi energy E_F, the function $(E - E_F)\mathrm{d}f_0/\mathrm{d}E$ cancels out when integrated. Hence, in order to get a non-vanishing contribution the partial conductivity must be asymmetrical about the Fermi energy. In other words, the conductivity must be either different for holes and electrons in the material, or an asymmetric function of energy. The latter can be realized for example by a strongly varying density of states around E_F. It can also be recognized that as the derivative function is finite only in a limited region around the Fermi energy, only electrons located here contribute significantly to the Seebeck coefficient.

While this illustrates nicely a dependence of thermoelectric effects on the electronic properties of the material, it is not the only way the electronic

---

[8] While the formally correct entity to use is the chemical potential, the near-equilibrium situation of the thermoelectric effects imply that it is sufficient to consider the Fermi energy.

structure comes into play. The conductivity of a material can be approximated to [39]

$$\sigma \propto \int \frac{\mathrm{d}f_0}{\mathrm{d}E} D(E) v_x^2(E) \mu(E) m^*(E) \mathrm{d}E \tag{2.5}$$

where $D(E)$ is the density of states, and v_x and μ and m^* are the speed, mobility and effective mass of the charge carriers, respectively.

Also the thermal conductivity is related to electronic properties as the amount of thermal energy each charge carrier transports, is given as its energy relative to the Fermi energy, or $E - E_F$. In fact, the electronic contribution to the thermal conduction is proportional to the electronic conductivity so that these properties are not easily decoupled[9], and a dependence on electronic structure is thus found in all factors governing the figure of merit (equation 2.3).

2.2.2 Thermoelectric materials and improvement of properties

Common thermoelectric materials and their dimensionless figure of merit zT as a function of operating temperature are shown in figure 2.6, which is adapted from [40]. Traditionally used thermoelectric materials are semiconductors such as $\mathrm{Si}_{0.8}\mathrm{Ge}_{0.2}$ and PbTe. The challenge of creating competitive thermoelectric devices has up to recently focused mostly on finding materials with a high zT. The last few years have brought about a new approach to this problem; rather than searching for materials with a certain property, one tries to design materials with the optimum electronic and thermal properties. Two such approaches have gained particular attention; nanostructuring of materials and the Phonon Glass - Electron Crystal (PGEC) concept.

One branch of nanostructuring aims at optimizing S or σ rather than the thermal properties. As both of these quantities are strongly connected to the electronic band structure of the material and to each other, individual tuning of them has proven difficult. By introduction of one or more reduced dimensions, the density of states can be altered significantly [41] and thus be another parameter by which $S^2\sigma$ can be tuned, for example shown for $\mathrm{Bi}_2\mathrm{Te}_3$ by Chen *et al.* [42].

---

[9] The thermal conductivity also has contributions from phonons that, especially in the case of semiconductors, need to be considered.

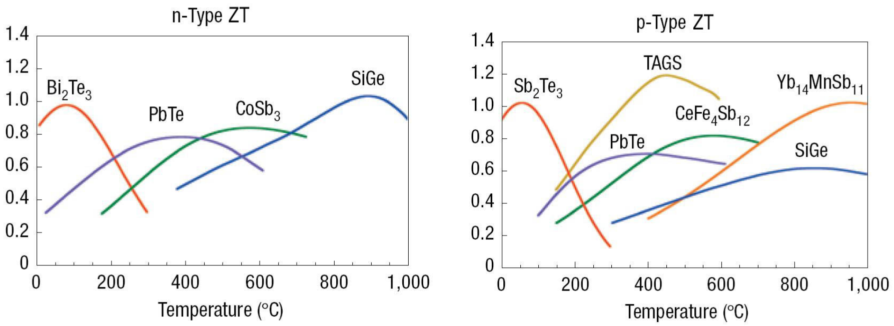

(a) (b)

Figure 2.6: *(Dimensionless) figure of merit ZT for some thermoelectric (a) n-doped and (b) p-doped materials as a function of temperature. Adapted from [40].*

There is also another side to nanostructuring thermoelectric materials, aiming at lowering the thermal conductivity by the introduction of surfaces and reduced dimensions which scatters phonons more than the charge carriers to yield a total gain in the figure of merit [43]. This approach is what has been termed the phonon glass - electron crystal approach, [44] to reflect the desired behavior of the material.

The skutterudite group of materials also belong the the PGEC way of improving thermoelectric properties. Skutterudites are large unit cell semiconductors with voids in the structure, and these voids hold the clue. By filling these voids with atoms with a covalent radius smaller than the cage itself, the filler atoms have a large degree of spatial freedom that can absorb phonons to lower the thermal conductivity [45]. This can be done without altering the electronic structure of the material considerably, thus preserving the values of S and σ. The PGEC approach also comprises mixed crystals or solid solutions of atoms with approximately the same electronic behavior [42].

2.3 Ferroelectricity

Ferroelectric materials are characterized not only by their ability to remain polarized without any external electric field, but also the possibility to change this direction of polarization. Macroscopically, the polarization can be viewed as continuous throughout the material, and this view enables a description of ferroelectricity in terms of phase transitions, domains and hysteresis loops. A detailed overview can be found for example in Lines and Glass [46] and will not be discussed further here.

While this phenomenological approach has been successful for interpreting ferroelectric properties in many circumstances for decades already, a microscopic understanding of the origin of ferroelectricity has been slower to develop. The 1990s brought changes to the understanding of ferroelectricity in more than one way. First, the so-called modern theory of polarization [47, 48] was conceived in which polarization is defined in terms of currents in the material upon transition to the ferroelectric state, thereby circumventing the troublesome point of having well-defined dipoles in the material that the classical theory relies on. Second, the introduction of density functional theory to the field made electronic structure predictions possible and lead to huge advances [49, 50], and such calculations are still considered invaluable although both atomic and electronic structure today can be probed experimentally at an atomic level [51].

Here, we will start with a very short and somewhat superficial introduction to relevant points from the theory of polarization, before considering how the atomic and electronic structure of a material are related to the subject of ferroelectricity in a more pictorial manner. We will focus our attention on ferroelectrics within the perovskite family, a large group of materials that are of both technological and scientific importance.

2.3.1 A short introduction to the theory of polarization

According to the traditional picture of ferroelectricity, the polarization $\boldsymbol{P}$ is defined as the sum of dipole moments in a unit cell divided by the cell volume. Implicitly this relies on the material to have well-defined units of dipoles that can be divided into localized contributions, a situation rarely encountered in real materials where the charge is delocalized and spread across the unit cell. Resta and Vanderbilt [52] showed in a clear manner how any attempt to directly relate charge density to the macroscopic measure of polarization is flawed. Also, with the rise of theoretical calculation schemes, it became clear that the experimental way of measuring polarization as a difference between two states[10] was inconsistent to a definition of

---

[10] For example, in a typical hysteresis loop measurement, one measures the two values of polarization at zero field and divides this value in half to find the spontaneous polarization of the system.

polarization as a single-value equilibrium property of the ferroelectric state of the crystal. The main idea behind the modern theory is that the polarization of a ferroelectric crystal can be defined in terms of an adiabatic charge current (with current density $\boldsymbol{j}(\mathrm{t})$) in the crystal upon transition from a centrosymmetric reference state to the ferroelectric state[11]:

$$\frac{d\mathbf{P}(\mathbf{t})}{dt} = j(t). \tag{2.6}$$

Quantum mechanically, currents are related to the phase of the wave function while charge density is dependent only on the modulus of the wave function, thus carrying no phase information and emphasizing the incompatibility of the two approaches. The total polarization is the sum of the electronic contribution and the ionic contribution, formulated by King-Smith and Vanderbilt [47] as

$$P = \frac{e}{2\pi V}\sum_n \psi_n \mathbf{R}, \tag{2.7}$$

ψ_n being the so-called Berry phase of the nth electronic band and R being the real-space lattice vector, while V is the primitive unit cell volume. It follows from this that the polarization is not a single-valued entity, but rather a multi-valued vector quantity with a modulo of $e\mathbf{R}/V$. Usually, this number is large enough to avoid confusion as to which value corresponds to the experimentally measured polarization. Using the Born effective charge tensor, defined as the polarization induced by a unit displacement u_s [53], a good approximation to the polarization can be expressed as

$$P \propto \sum_s Z_s^* u_s, \tag{2.8}$$

Z_s^* being the diagonal components of the Born effective charge tensor along the displacement direction [54]. The deviation from linearity and thus this equation is at maximum 10-20% [52].

2.3.2 Structural and electronic characteristics of ferroelectrics

Crystallographically, any ferroelectric material has to belong to a polar space group. The constraint that a ferroelectric material, unlike a pyroelectric material, can also change the direction of polarization into two or more

---

[11] In general, the currents are evaluated under the relevant conditions, such as under the influence of strain (in the case of piezoelectric materials) or electric fields (as in the case of a polarizable dielectrics).

equivalent directions implies further that the symmetry of the unit cell must be close to a higher symmetry, so that the ferroelectric (polar) phase can be regarded as a small symmetry-breaking distortion of the non-ferroelectric (non-polar) phase. Usually, the non-polar phase is the high-temperature phase of the ferroelectric material, above the phase transition (Curie) temperature T_c. This transition temperature varies from very low (less than 1K) to high temperatures, and can in some cases be higher than the melting point of the material.

There are a number of classifications and divisions of ferroelectric materials, depending on the underlying mechanism for polarization or the ferroelectric behavior. One often distinguish between *conventional* and *electronic* ferroelectrics based on the origin of ferroelectricity. In the former, it is the atomic arrangement of the various atomic species in the lattice or their covalent bonding that gives rise to the polarization, while in the latter the ferroelectricity is caused by electronic correlation effects such as spin - and charge ordering [55].

Within the conventional ferroelectrics, a number of different mechanisms can contribute to the polarization. In ferroelectric $BaTiO_3$, the origin of ferroelectricity is often termed a ”polarization catastrophe” and is a result of hybridization effects lowering the energy more than the ionic energy increase upon transition to a non-centrosymmetric unit cell. Another example is the lone pair of electrons found to be a reason for ferroelectricity in both $PbTiO_3$ and $BiFeO_3$. Depending upon the behavior above T_c and the nature of the polar distortion, conventional ferroelectrics are further subdivided into two categories: *Order-disorder* ferroelectrics are characterized by the unit cells of the high-temperature phase having unordered individual dipole moments that on a macroscopic level averages out. On the other hand, *displacive* ferroelectrics have no dipole moments until crossing the critical temperature.

The rare earth manganites, of which $HoMnO_3$ is a member, are examples of spin ordered ferroelectrics in which polarization often[12] is magnetically induced. Other examples of electronic ferroelectrics include $LaFe_2O_4$, predicted to have a polarization due to ordering of mixed valence iron ions [56]. Usually, the polarization is an order of magnitude larger in conventional ferroelectrics than in electronic ferroelectrics.

The group of conventional ferroelectrics also more or less corresponds to the group of *proper* ferroelectrics, in which the polarization is the primary order parameter. Correspondingly, most electronic ferroelectrics also belong to

---

[12] Though not for $HoMnO_3$

the group of *improper* ferroelectrics, in which the polarization is a secondary effect arising from some other form of ordering[13].

Both $PbTiO_3$ and $BiFeO_3$ are examples of one of the most well-known group of materials, the perovskites (ABX_3). This class of materials takes its name from the cubic mineral $CaTiO_3$, although the perovskite family is now considered to encompass also related, but distorted structures [58]. The behavior of perovskites is diverse and rich in exotic phenomena, ranging from colossal magnetoresistance [59] to multiferroism and superconductivity [58]. Many ferroelectric compounds have also been found within the perovskite family, including what has become the ”prototype” ferroelectric barium titanate $BaTiO_3$.

The non-polar perovskite unit cell is cubic and belongs to space group $Pm\bar{3}m$ and is shown in figure 2.7, together with some of the possible distortions of this group of materials.

The B cation is octahedrally coordinated with oxygen on the octahedral positions, while the A cation is 12-fold coordinated in between the octahedra. Considering conventional ferroelectric perovskites, they display a displacement of the central B cation along one of the major crystallographic axes, causing a shift in the cation sublattice relative to the anion sublattice and thus a net polarization. Displacement along the (cubic) [001] direction leads to a tetragonal unit cell (figure 2.7(b)), a displacement along [110] to an orthorhombic unit cell (figure 2.7(c)) while a displacement along [111] leads to a rhombohedral unit cell (figure 2.7(d)). It has been verified that the displacement scales almost linearly with the polarization of the material, as stated in equation 2.8 [52, 54].

Turning to the electronic structure of ferroelectric perovskites, they are mainly ionic compounds with nominal valence charges being usually $A^{1+}B^{5+}(O^{2-})_3$, $A^{2+}B^{4+}(O^{2-})_3$ or $A^{3+}B^{3+}(O^{2-})_3$. The covalent contribution to bonding is small, but defining for the ferroelectric properties of conventional ferroelectric perovskites: It has been shown theoretically for several perovskites, including $BaTiO_3$ and $KNbO_3$, that the cause of the displacement of the cation sublattice is a covalent bonding between O p and B cation d electrons, and that upon removal of this covalent bond the ferroelectricity vanished [49, 54, 60]. Figure 2.8 is adapted from [54] and shows as an example charge density plots of the O p electrons of $KNbO_3$ in

---

[13] While it should be noted that $YMnO_3$, while being classified as an improper ferroelectric, is not an electronic ferroelectric as the primary order parameter is coupled to a (non-polar) structural instability [57].

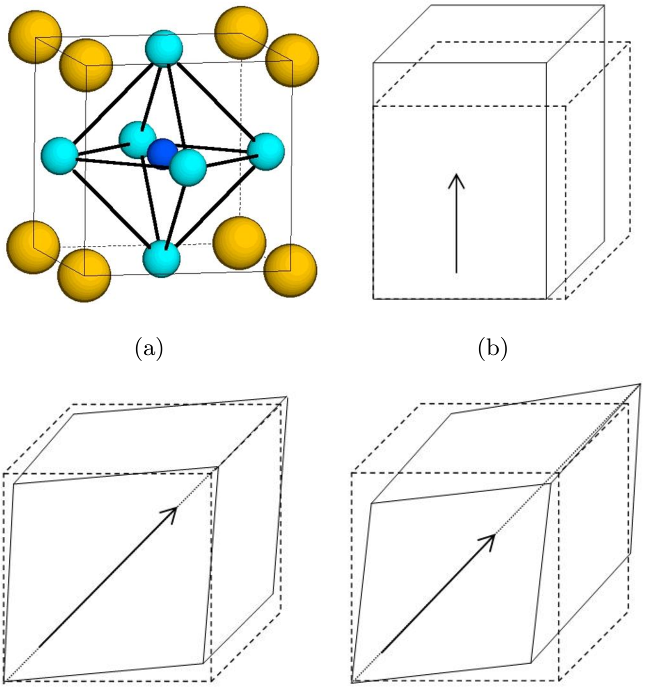

(a) (b)

(c) (d)

Figure 2.7: *(a) Perovskite unit cell. A atoms are shown in yellow, B atoms in blue and X atoms in green. The octahedral coordination of B atoms is emphasized by black lines denoting the X - X bonds. (b) - (d) Tetragonal, orthorhombic and rhombohedral distortions of the cubic unit cell in (a), respectively. The arrows indicate the direction of polarization for each of the distortions.*

the case of the centrosymmetric (non-ferroelectric) structure and ferroelectric structure, and the same two cases with the covalency turned off, clearly demonstrating the effect of covalency.

In perovskites, the values of the Born effective charge tensor (discussed in section 2.3.1) also holds clues to the origin of ferroelectricity. Using a rigid-ion model, the values would be equal to the nominal charges of the ions (i.e. -2 for O) while in practice, "anomalous" high values are found for some of the ions in the material. Using again $KNbO_3$ as an example, Posternak *et al* [54] found values of 0.8 (K), 9.1 (Nb) and -6.6 and -1.7 for the two O positions in the unit cell. The unexpectedly high values of Nb and O is related to the charges flowing through the crystal between these atoms as

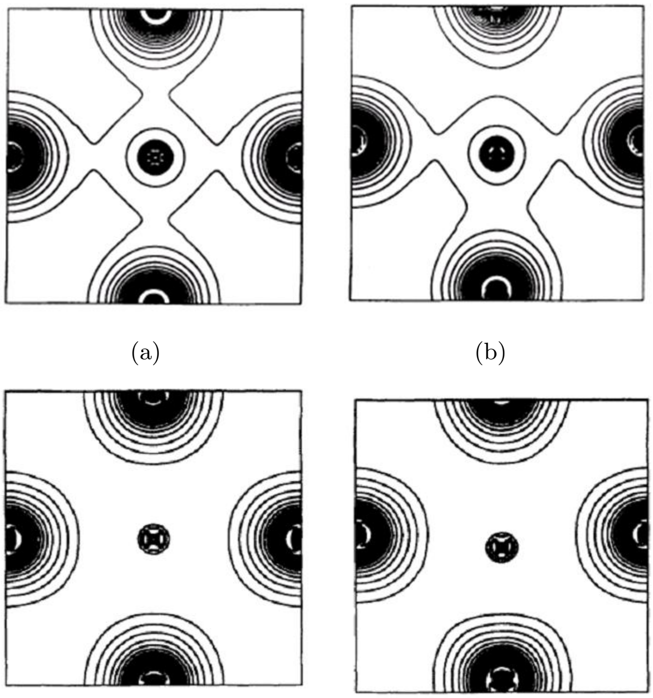

(a) (b) (c) (d)

Figure 2.8: *Calculated charge density maps of $KNbO_3$. (a) and (b) shows the centrosymmetric and ferroelectric state, respectively, while the same two situations are shown in (c) and (d) with the covalent O - Nb bond suppressed. In all figures the map is through the pseudocubic {200} plane containing Nb and four oxygen atoms. The figure is adapted from [54].*

the material enters the ferroelectric state, and is again strongly related to the covalent part of the bond between these atoms [54]. It is worth noticing that this tendency to form covalent O p - B cation d bonds and thus polarize in this way seems to be reserved perovskites with the B metal atom in d^0 configuration [61, 62, 63].

Thus, the connection between electronic structure and ferroelectricity is clearly present both in conventional and electronic ferroelectrics. In later chapters, various conventional ferroelectrics will be studied both with regards to the connection between bonding and ferroelectricity, and the domain structure of ferroelectric nanorods.

References

[1] S Elliott: *The physics and chemistry of solids.* John Wiley and Sons, Chichester (2000).

[2] Williams DB and Carter CB: *Transmission Electron Microscopy.* Springer Science, New York (2009).

[3] Egerton RF: *Electron Energy-Loss Spectroscopy in the Electron Microscope.* Plenum Press, New York (1996).

[4] Muller DA: *Structure and bonding at the atomic scale by scanning transmission electron microscopy.* Nature Mat **8**, 263 (2009).

[5] Garvie LAJ, Craven AJ, Brydson R: *Use of electron energy-loss near-edge fine-structure in the study of minerals.* Amer. Miner. **79**, 411 (1994).

[6] Keast VJ, Scott AJ, Brydson R *et al.*: *Electron energy-loss near-edge structure - a tool for the investigation of electronic structure on the nanometre scale.* J. Microsc. **203**, 135 (2001).

[7] Malis T, Cheng SC and Egerton RF: *EELS log-ratio technique for specimen-thickness measurement in the TEM.* J. electr. micro. techn. **8**, 193 (1988).

[8] Schaffer B, Hohenester U, Trugler A, *et al.*: *High-resolution surface plasmon imaging of gold nanoparticles by energy-filtered transmission electron microscopy.* Phys. Rev. B **79**, 041401 (2009).

[9] Howe JM and Oleshko VP: *Application of valence electron energy-loss spectroscopy and plasmon energy mapping for determining material properties at the moment.* J. Electr. Microsc. **53**, 339 (2004).

[10] Rez P and Muller DA: *The theory and interpretation of electron energy loss near-edge fine structure.* Annu. Rev. Mater. Res. **38**, 535 (2008).

[11] Brydson R, Sauer H; Eengel W *et al.*: *EELS as a fingerprint of the local chemical coordination of light-elements.* Microsc. Microanal. Microstruct. **2**,159 (1991).

[12] Pearson DH, Ahn CC and Fultz, B: *White lines and* d*-band occupancies for the 3*d *and 4*d *transition metals.* Phys. Rev. B **47**, 8471 (1993).

[13] Leapman RD, Grunes LA, Fejes PL: *Study of the* $L_{2,3}$ *edges in the 3*d *transition metals and their oxides by electron-energy*

loss spectroscopy with comparison to theory. Phys. Rev. B **26**, 614 (1982).

[14] Paterson JH and Krivanek OL: *ELNES of 3d transition-metal oxides. 2. variations with oxidation-state and crystal-structure.* Ultramicr. **32**, 319 (1990).

[15] van Aken PA, Liebscher B, Styrsa VJ: *Quantitative determination of iron oxidation states in minerals using Fe L-2,L-3-edge electron energy-loss near-edge structure spectroscopy.* Phys. Chem. Miner. **25**, 323 (1998).

[16] Egerton RF: *Electron energy-loss spectroscopy in the TEM.* Rep. Prog. Phys. **72**, 016502 (2009).

[17] van Benthem K, Elsässer C and Rühle M: *Core-hole effects on the ELNES of absorption edges in* $SrTiO_3$. Ultramicr. **96**, 509 (2003).

[18] Mo S-D and Ching WY: Ab initio *calculation of the core-hole effect in the electron energy-loss near-edge structure.* Phys. Rev. B **62**, 7901 (2000).

[19] Lie K, Brydson R and Davock H: *Band structure of* TiB_2*: Orientation-dependent EELS near-edge fine structure and the effect of the core hole at the B* K *edge.* Phys. Rev. B **59**, 5361 (1999).

[20] Browning ND, Yuan J and Brown LM: *Real-space determination of anisotropic electronic-structure by electron-energy loss spectroscopy.* Ultramicr. **38**, 291 (1991).

[21] Lie K, Høyer and Brydson R: *Theoretical site- and symmetry-resolved density of states and experimental EELS near-edge spectra of* AlB_2 *and* TiB_2. Phys. Rev. B **61**, 1786 (2000).

[22] Schattshneider P, Hebert C and Jouffrey B: *Orientation dependence of ionization edges in EELS.* Ultramicr. **86**, 343 (2001).

[23] Kirkland EJ: *Some effects of electron channeling on electron energy loss spectroscopy.* Ultramicr. **102**, 199 (2005).

[24] Seabourne CR, Scott AJ, Brydson R *et al.*: *A systematic approach to choosing parameters for modelling fine structure in electron energy-loss spectroscopy.* Ultramicr. **109**, 1374 (2009).

[25] Ankudinov AL, Ravel B, Rehr JJ and Conradson SD: *Real-space multiple-scattering calculation and interpretation of x-*

ray-absorption near-edge structure. Phys. Rev. B **58**, 7565 (1998).

[26] Moreno MS, Jorissen K and Rehr JJ: *Practical aspects of electron energy-loss spectroscopy (EELS) calculations using FEFF8.* Micron **38**, 1 (2007).

[27] Ravel B: *A practical introduction to multiple scattering theory.* J. All. Comp. **401**, 118 (2005).

[28] Spence JCH and Zuo JM: *Electron microdiffraction.* Plenum press, New York (1992).

[29] Liu P and Skogsmo J: *Space-group determination and structure model for kappa-Al_2O_3 by convergent-beam electron-diffraction (CBED).* Acta Cryst. B **47**, 425 (1991).

[30] Zuo JM, Kim M and Holmestad R: *A new approach to lattice parameter measurements using dynamic electron diffraction and pattern matching.* J Electr. Microsc. **47**, 121 (1998).

[31] Morniroli JP: *CBED and LACBED characterization of crystal defects.* J. Microsc. **223**, 240 (2006).

[32] Zuo JM, Kim M, O'Keeffe M *et al.*: *Direct observation of d-orbital holes and Cu-Cu bonding in Cu_2O.* Nature **401**, 49 (1999).

[33] Humphreys CJ: *The scattering of fast electrons by crystals.* Rep. Prog. Phys **42**, 122 (1979).

[34] Zuo JM and Spence JCH: *Coherent electron nanodiffraction from perfect and imperfect crystals.* Phil. Mag A **68**, 1055 (1993).

[35] Zuo JM and Weickenmeier A: *On the beam selection and convergence in the Bloch wave method.* Ultramicr. **57**, 375 (1995).

[36] Zuo JM: *Electron detection characteristics of slow-scan CCD camera.* Ultramicr. 66, 21 (1996).

[37] Friis J, Marthinsen K, Holmestad R: *Retrieval of anisotropic displacement parameters in Mg from convergent beam electron diffraction.* Inst. Phys. Conf. Ser. **165**, 307 (2003).

[38] Nolas GS, Sharp J, Goldsmid HJ: *Thermoelectrics: basic principles and new materials developments.* Springer Verlag, Berlin (2001).

[39] Dugdale JS: *The electrical properties of metals and alloys.* E Arnold, London (1977).

[40] Snyder GJ and Toberer ES: *Complex thermoelectric materials.* Nature Mater. **7**, 105 (2008).

[41] Dresselhaus MS, Chen G, Tang MY *et al.*: *New directions for low-dimensional thermoelectric materials.* Adv. Mater **19**, 1043 (2007).

[42] Chen G, Dresselhaus MS, Dresselhaus G, Fleurial J-P and Caillat T: *Recent developments in thermoelectric materials.* Int. Mater. Rev **48**, 45 (2003).

[43] Lan Y, Minnich AJ, Chen G, Ren Z: *Enhancement of Thermoelectric Figure-of-Merit by a Bulk Nanostructuring Approach.* Adv. Func. Mater. **20**, 357 (2010).

[44] Slack, GA in *CRC handbook of thermoelectrics* (ed. D. M. Rowe) CRC Press, Boca Raton (1995).

[45] Sales BC, Mandrus D, Chakoumakos BC, Keppens V, and Thompson RJ: *Filled skutterudite antimonides: Electron crystals and phonon glasses.* Phys. Rev. B **56**, 15081 (1997).

[46] Lines ME and Glass AM: *Principles and Applications of Ferroelectrics and Related Materials.* Oxford university press, New York (1977).

[47] King-Smith RD and Vanderbilt D: *Theory of polarization of crystalline solids.* Phys. Rev. B **47**, 1651 (1993).

[48] Resta R: *Macroscopic polarization in crystalline dielectrics: The geometric phase approach.* Rev. Mod. Phys **66**, 899 (1994).

[49] Cohen RE and Krakauer H: *Lattice dynamics and origin of ferroelectricity in* $BaTiO_3$*: Linearized-augmented-plane-wave total-energy calculations.* Phys. Rev. B **42**, 6416 (1990).

[50] Neumann T, Borstel G, Scharfschwerdt C and Neumann M: *Electronic structure of* $KNbO_3$ *and* $KTaO_3$. Phys. Rev. B **46**, 10623 (1992).

[51] Browning ND and Pennycook SJ: *Atomic-resolution electron energy-loss spectroscopy in the scanning transmission electron microscope.* J. Microsc. **180**, 230 (1995).

[52] Resta R and Vanderbilt D: *Theory of polarization: A moder approach.* In *Physics of ferroelectrics: a modern perspective.* Rabe KM, Ahn CH and Triscone JM (eds.), Springer Verlag, Berlin (2007).

[53] Resta R: *Dynamical charges in oxides: recent advances.* J. Phys. Chem Solids **61**, 153 (2000).

[54] Posternak M, Resta R and Baldereschi A: *Role of covalent bonding in the polarization of perocskite oxides: The case of* $KNbO_3$. Phys. Rev. B **50**, 8911 (1994).

[55] Ishihara S: *Electronic ferroelectricity and frustration.* J. Phys. Soc. Jpn. **79**, 011010 (2010).

[56] Ikeda N, Ohsumi H, Ohwada K *et al.*: *Ferroelectricity from iron valence ordering in the charge-frustrated system* $LuFe_2O_4$. Nature **436**, 1136 (2005).

[57] Fennie CJ and Rabe KM: *Ferroelectric transition in* $YMnO_3$ *from first principles.* Phys. Rev. B **72**, 100103(R) (2005).

[58] Goodenough JB: *Electronic and ionic transport properties and other physical aspects of perovskites.* Rep. Prog. Phys. **67**, 1915 (2004).

[59] Ramirez AP: *Colossal magnetoresistance.* J Phys. Cond. Mater. **9**, 8171 (1997).

[60] Cohen RE: *Origin of ferroelectricity in perovskite oxides.* Nature **358**, 136 (1992).

[61] Khomskii DI: *Different ways to combine magnetism and ferroelectricity.* J. Magn. Magn. Mater. **306**,1 (2006).

[62] Rondinelli JM, Eidelson AS and Spaldin NA: *Non-*d^0 *Mn-driven ferroelectricity in antiferromagnetic* $BaMnO_3$. Phys. Rev. B **79**, 024102 (2009).

[63] Bhattacharjee S, Bousquet E and Ghosez P: *Engineering Multiferroism in* $CaMnO_3$. Phys. Rev. Lett. **102**, 117602 (2009).

Chapter 3

Electronic structure of Skutterudites

3.1 Introduction

In this chapter, I report the results of an EELS investigation of phosphorus skutterudites. Skutterudites are thermoelectric semiconductors, and have adopted their name from the mineral $CoAs_3$. They are cubic, large unit cell materials belonging to space group $Im\bar{3}$, with the binary formula MX_3, M=Co, Rh, Ir, Ni and X=P, As, Sb. Depending on the choice of origin, the crystal structure can be imagined either as an M cubic network filled with X_4 squares in three different orientations (figure 3.1(a)), or as tilted corner-sharing X octahedra centered on an M atom (figure 3.1(b)) [1]. The X atoms are almost tetrahedrally coordinated with two nearest X and two nearest M neighbors. The crystallographic *a* site is left empty in the binary skutterudites, leaving large voids that can be filled preferably with rare earth atoms, yielding ternary skutterudite compounds RM_4X_{12}. These filler atoms are referred to as rattlers, as their covalent radii are usually smaller than the surrounding cage so that the atoms are allowed spatial freedom to "rattle" around. Up until recently, this is believed to be the cause of the reduction in thermal conductivity and thus increased thermoelectric performance of such ternary skutterudites, however some recent studies suggest that the reason is slightly more complicated [2, 3].

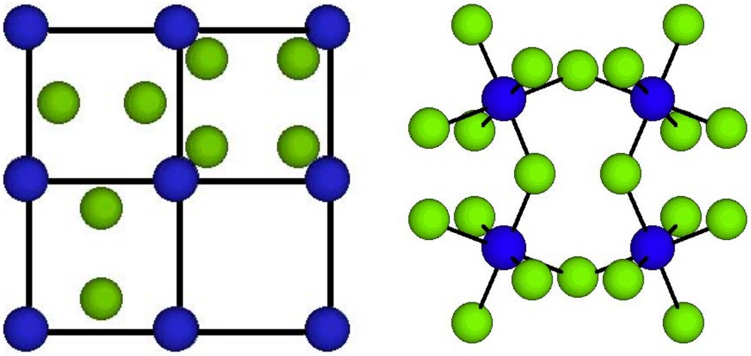
(a) (b)

Figure 3.1: *Crystal structure of skutterudites: (a) Part of a skutterudite unit cell showing the M atom (blue) cubic network and the X squares in three different orientations along the three cubic axes. The fourth M cube is empty in the unfilled structures, and houses the rattler atom in the filled structures. (b) Alternative view of skutterudite unit cell, showing the M atoms octahedrally surrounded by X atoms and the tilting of the octahedra.*

The traditional picture of bonding in skutterudites involves primarily covalent bonding with little contribution from ionic bonding [4]. The somewhat simple Dudkin model [5] predicts that out of the five X valence electrons (s^2p^3), two form covalent bonds to each of the two X neighbors, while the remaining three are shared between the two nearest M atoms. The octahedrally coordinated M atoms donate three out of their nine valence electrons (d^7s^2) to the M-X bond, which is mediated through d^2sp^3 hybrid orbitals. The X-X bonds are mediated through σ orbitals involving mainly p electrons, as suggested by the 90° X-X-X bond length [1]. In total, this gives nominal charges of $M^{3+}X^{1-}$.

Any further insight into the electronic structure of skutterudites awaited the introduction of density functional theory to this field around 1990. Especially calculations by Jung *et al.* [6] started a debate that is still not completely settled upon the importance of the X_4 units. Their calculations showed these highest occupied band of $LaFe_4P_{12}$ to originate from P states within these units, while later calculations [7, 8] and experimental studies [9] have predicted contributions also from M d states in the highest valence bands. The importance of the X states is however confirmed by several studies [10, 11, 12, 13] predicting a single X band crossing a band gap near E_F, which is thus responsible for many of the electronic properties. The influence of the M d states is important also in another respect, in that they bond covalently to X p states. The overall covalent nature of the bonds is decisive for the thermoelectric performance of skutterudites, as it influences both thermal and electronic properties [1, 14]. The degree of covalency is strongly connected to the electronegativity of the involved atomic species and the charge transfer between them [14], which has been investigated in some recent studies [9, 14, 15, 16, 17] concluding that there is a small charge transfer from the M atoms to the X atoms. It is interesting to note that the charge density of $CoSb_3$ has been investigated both theoretically [9] and by X-ray diffraction [15] through charge density maps, which complements nicely the use of spectroscopic techniques [8, 14, 16].

The above discussion has made no comment as to the differences between the various groups of skutterudites. Though very similar in many aspects, and especially regarding the electronic structure, there are a few differences worth noticing. A distinction based on the X atoms can be made, giving three main groups of phosphide, arsenide and antimonide skutterudites. Of these, the antimonides are by far the most studied, due to their better thermoelectric performance [18, 19]. This is first and foremost due to a relatively low value of the thermal conductivity[1], induced by the heavy mass of the Sb atoms. Also the electronic structure of the antimonides is worth mentioning. Together with the phosphides, and unlike the arsenides, the X band crossing the band gap near E_F is linear in appearance rather than parabolic [7]. This causes unusual properties of the charge carriers residing there and thus influences also the Seebeck coefficient and electronic transport properties. Generally, skutterudites are excellent hole conductors with mobilities higher than typical semiconductors such as Si, Ge, and GaAs [1], due to a strong asymmetry in the density of states near E_F where the density of states at the top of the valence band is rapidly varying with energy.

So far, the discussion has been on binary (unfilled) skutterudites. In contrast to the essentially covalent M-X and X-X bonds, the filler atoms are assumed to form ionic bonds to the rest of the structure. Usually, the rare earth filler atom is assumed to be in a 3+ valence state, donating three electrons to the $[M_4X_{12}]$ complex. Using the commonly studied $LaFe_4P_{12}$ as an example, the La atom thus contribute with only three of the four less electrons provided by Fe than in the binary CoP_3 compound. It is typical that the hypothetical compound $LaCo_4P_{12}$ cannot form, so that fully substituted ternary skutterudites contain the M elements Fe, Ru and Os. These ternary compounds are charge deficient compared to binary skutterudites, and are thus hole conductors under the assumption that the electronic structure is otherwise unaltered. To some extent, this assumption is verified and the missing electron is found as a hole in the valence band [8]. Even if fully filled skutterudites with M = Co, Rh, Ir do not form, most of these structures tolerate filling up to a certain degree. For example, it has been demonstrated that at least one fifth of the voids in CoP_3 can be filled with La [20]. The missing electron of fully filled skutterudites can be charge compensated either by substitution on M or X sites (see e.g. [21, 22]). In total, this gives a very large and steadily increasing family tree of unfilled, partially and fully filled skutterudites, many of which have only been superficially studied and tested for thermoelectric and other properties.

---

[1] With values ranging from 5-10 W/mK for $CoSb_3$, compared to 14.5 for $CoAs_3$ and 18.5 for CoP_3. See [1] and references therein.

3.2 Paper 1: Electron energy loss spectroscopy of the $L_{2,3}$ edge of phosphorus skutterudites and electronic structure calculations

This paper was published in *Physical Review B*, 2009, and discusses the differences in electronic structure of various phosphorus-based skutterudites. Results from initial measurements were reported in another paper, published in *Micron* [23].

A main conclusion of the work is that from the perspective of the phosphorus atoms, the differences are small even in the case of the filled skutterudite $LaFe_4P_{12}$ and the metallic NiP_3 having one excess electron compared to CoP_3. Main differences are interpreted in terms of the electronegativity of the involved atoms, and compared to the more studied and in many ways similar Si compounds. In addition, two calculation schemes were tested and, despite their differences and simplifications, found to reproduce the experimental data to a high degree.

I have performed the experimental EELS work and the interpretation of the data in this article, while DFT and RSMS calculations were performed mainly by Espen Flage-Larsen and Øystein Prytz, respectively.

3.3 *Paper 2:* Experimental and theoretical study of electron density and structure factors in $CoSb_3$

This paper discusses the struggles and outcomes of CBED experiments on $CoSb_3$, and has been accepted for publication in *Ultramicroscopy*. It represents what should have been a main topic of this PhD, but has to settle for representing the start and the end of the PhD instead: The experiments and initial refinements were done at an early stage and given up on and forgotten until we were notified of a special issue of *Ultramicroscopy* in the honor of John Spence, one of the founders of CBED refinements and long-time collaborator of many in the TEM group. The CBED patterns were then re-examined with indispensable help of Jesper Friis, and after having overcome several obstacles they finally yielded two refinable structure factors.

The experimental CBED patterns used for the paper were recorded during a one-week stay at Poitiers, France, together with Prof. Jérôme Pacaud, while the post-processing was done in Trondheim. The difficulties of refining structure factors from large unit cell systems is discussed in detail, while the refinement results of two structure factors are reported and the best fits compared to experimental X-ray structure factors of Finn Krebs Larsen and co-workers, Aarhus, Denmark, and also theoretical values obtained from DFT by Espen Flage-Larsen.

Is not included due to copyright

Chapter 4

Electronic structure of $BiFeO_3$ and related compounds

4.1 Introduction

Magnetic and ferroelectric materials are already being separately employed at a large scale in memory technology, as conventional magnetic memory devices and the more recent ferroelectric memory devices [1]. The combination of the two phenomena opens up new possibilities within memory storage, for example in four-state memory devices [2]. Even more intriguing is the idea that if the materials exhibit a strong, preferably linear, magnetoelectric coupling, bits could be written electrically and read magnetically [3]. Such a device would combine the best from the two worlds, as writing bits is faster when done electrically while reading bits is easiest done magnetically. The high scientific interest in multiferroic materials is seen in the ever increasing number of articles related to the subject: The record count for the term ”multiferroic” on ISI Web of Science has increased from 1 in 2000 to a preliminary all-time high of 630 in 2009. Of the increasing number of multiferroic compounds known [4, 5, 6], very few are found to have a combination of magnetic and ferroelectric properties at or near room temperature.

In the family of multiferroics, bismuth ferrite (BiFeO$_3$) stands out as it is simultaneously ferroelectric and antiferromagnetic at room temperature and up to the Néel temperature at about 643 K (and with an even higher ferroelectric Curie temperature of about 1100 K). Moreover, a magnetoelectric coupling has been predicted first theoretically [7] and later proven experimentally [8, 9]. The complex and intriguing nature of the electron behavior in bismuth ferrite is the focus of research groups around the world, while another branch of scientists are working to improve the (especially magnetic) properties. Bismuth ferrite in thin film form in particular has been in the center of attention [10, 11], however for this study we will focus upon the bulk properties.

Looking into the crystal structure, bismuth ferrite is a rhombohedrally distorted perovskite [12, 13, 14] belonging to space group $R3c$ (see figure 2.7(a) and 2.7(d)). The unit cell is elongated in the pseudocubic [111] direction, to a rhombohedral angle of 59.35°. Oxygen octahedra are rotated antiferrodistortively around the pseudocubic [111] axis along all three cubic axes, so that the pseudocubic unit cell is half the size (including only one rotation direction) of the rhombohedral cell. Two pseudocubic cells are shown in figure 4.1. The Fe and Bi atoms are shifted from their position in the cubic perovskite structure along the pseudocubic [111] axis, with the Bi displacement being larger than the Fe displacement.

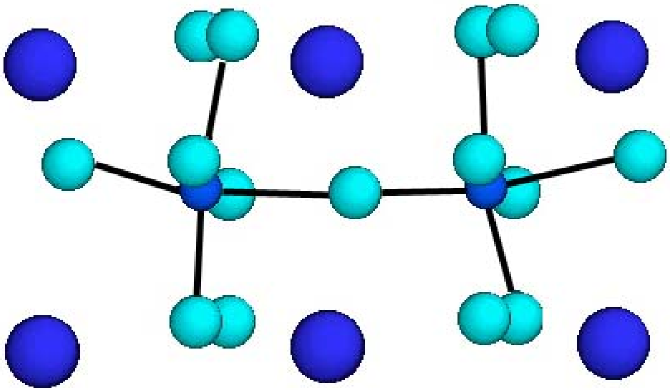

Figure 4.1: *Two pseudocubic unit cells of BiFeO*$_3$*, showing the rotation of the oxygen (green) octahedra and the non-centrosymmetric placement of the Fe (small blue) and Bi (large blue) atoms.*

The electronic structure and origin of ferroelectricity in bismuth ferrite is more complex than the situation outlined for typical perovskites in section 2.3.2. The covalent O p - B cation d bonds responsible for ferroelectricity in $KNbO_3$, $BaTiO_3$ and partially in $PbTiO_3$ do not seem to play a very large role in $BiFeO_3$ [15]. There is one aspect of $PbTiO_3$ and bismuth ferrite that is similar, however. Both Pb^{2+} and Bi^{3+} are known to have a lone pair of electrons that for a long time was believed not to participate in bonding. This electron pair occupies a large portion of space, distorting the charge balance of the atom and drives the atom cores to their distorted positions, thereby breaking local inversion symmetry. *Ab initio* calculations [16], have shown that as much as 98 % of the polarization is due to this off-centered Bi atom. The spontaneous polarization of bismuth ferrite has been measured to about 100 $\mu C/cm^2$ [17], higher than the corresponding value of about 75 $\mu C/cm^2$ found in lead titanate[1] [21].

The magnetic structure of bismuth ferrite is on the macroscopic scale antiferromagnetic, however the situation is more complex on an atomic scale. The spins are perpendicular to the polar pseudocubic [111] direction, and canted to yield a cycloidal spin ordering with a period of 62 nm (see [22] for further details).

Less understood than the magnetic and electric properties, but increasingly

---

[1] Although initial measurements predicted a much lower value, probably due to leakage currents and impurities. [18, 19, 20]

well documented, is the magnetoelectric coupling [7, 16], describing any coupling of magnetic and electric properties. While the magnetism is connected to the iron atoms, the ferroelectricity is attributed to a shift of the bismuth atoms in the pseudocubic [111] crystallographic direction. Adding to this picture is a series of recent measurements on substituted bismuth ferrite, showing that the ferroelectric phase transition temperature, the Curie temperature (T_C), decreases upon substitution on iron site [23, 24]. These phenomena have been studied by DFT calculations [16, 25] that have predicted that there are details to the image of conventional bonding in perovskites that needs to be modified in the case of bismuth ferrite, while few experimental studies have been published on the electronic structure so far.

What is known about the electronic structure, is that bismuth ferrite is a semiconductor with primarily ionic bonding, the nominal charges being 3+ for Bi and Fe and 2- for O. There is, however, a small covalent contribution that has important consequences for the material, since a purely ionic perovskite would attain a centrosymmetric structure. The role of the Bi $6s^2$ lone pair of electrons has been mentioned previously, and illustrates the influence of covalency nicely: With only s electrons, the $6s^2$ lone pair would be symmetrically distributed around the atom core so that contributions from either Bi $5p$ states or O p states are expected. Covalent bonds have been predicted theoretically between both Fe - O and Bi - O [16], as illustrated by the charge density map of figure 4.2.

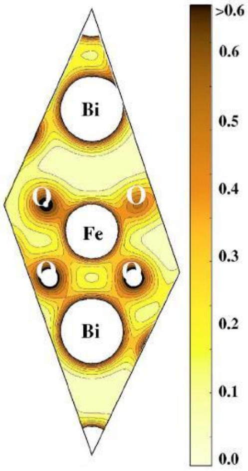

Figure 4.2: *Calculated charge density map of BiFeO$_3$. The figure is adapted from Ravindran* et al. *[16].*

The motivation for substitution on both cation sites in this study has primarily been nurtured by the need for a better understanding of the role of the different cations. So far, the majority of the studies on substituted compounds have focused on the multiferroic properties, and ferroelectric properties in particular, finding an enhancement of ferroelectric response both in La doped [26, 27, 28, 29] and Mn doped [24, 30] bismuth ferrite. It is to date not clear whether this enhancement is a property of the bulk phases, or a result of less secondary phases and generally more perfect crystals [27]. The study of the electronic structure of cation substituted bismuth ferrite may therefore aid the understanding of the properties of both pure bismuth ferrite as well as the substituted compounds themselves.

4.2 *Paper 3:* Electronic structure of multiferroic $BiFeO_3$ and related compounds: Electron energy loss spectroscopy and density functional study

The following paper was published in *Physical Review B*, 2010, and is, as the title suggest, a joint experimental and theoretical study of multiferroic bismuth ferrite and the two isostructural cation-substituted compounds $Bi_{0.9}La_{0.1}FeO_3$ and $BiFe_{0.7}Mn_{0.3}O_3$. It started out as a "take whatever material is available and see if I can get something out of it" kind of project, and ended up with results far exceeding what I had hoped for, much thanks to excellent and eager co-authors.

The work sheds light on the interplay of the various atomic species in the structure, to show that the A and B site cations are more coupled than previously recognized, and suggests that this may be due to small, but finite covalent cation-oxygen bonds. This has potentially wide-reaching consequences, as we show that subtle changes in bonding and electronic behavior are more important than commonly recognized and could potentially be a part of the explanation of the magnetoelectric coupling in these and similar materials.

I have performed the experimental EELS work and the RSMS calculations in this article as well as the interpretation of the results, while X-ray diffraction and calorimetric measurements have been performed by Sverre M. Selbach and the DFT calculations by Ponniah Ravindran.

Is not included due to copyright

Chapter 5

Domain structure and related properties of $PbTiO_3$ nanorods

5.1 Introduction

In this chapter, I explore the structure of hydrothermally grown lead titanate (PbTiO$_3$) nanorods by various TEM techniques. Lead titanate is a well-known ferroelectric material which is much studied, especially due to its close relation to the commercially much employed (Pb,Zr)TiO$_3$. Syntheses of lower-dimensionality ferroelectric materials in general have so far been dominated by thin films, perhaps due to difficulties in synthesizing especially 1D structures. The study of 1D ferroelectrics are interesting both from a scientific and a technological point of view: With the increasing demand for miniaturization of electronic devices, there is a constant search for ways to increase storage density in e.g. memory devices. Low-dimensionality ferroelectric systems is one of the directions currently investigated to achieve this [1, 2, 3, 4].

Scientifically, there are numerous studies related to the size dependence of ferroelectric phenomena. Coarsely speaking, these phenomena can be divided in two by the length scales at which they set in. One is related to the possible disappearance of ferroelectricity at a small number of unit cells of material. Early studies suggested that a critical size existed below which ferroelectricity disappeared [5, 6], while later studies suggest that rather than being an intrinsic material property, it rather depends upon mechanical and electrical boundary conditions [4, 7]. The other is related to the size of ferroelectric domains, and it has been shown [8] that the domain size is dependent on the size of the material up to material thicknesses of several hundred nanometers.

At room temperature, lead titanate adopts a tetragonal perovskite structure (figure 2.7(a) and 2.7(b)), with Ti octahedrally surrounded by O atoms. It has a Curie temperature of 490 °C, above which it is paralelectric. The origin of ferroelectricity in lead titanate is slightly more complicated than in the case of the prototype ferroelectric BaTiO$_3$, with contributions both from the covalent bond between O p - Ti d states (as in the prototype displacive perovskites BaTiO$_3$ and KNbO$_3$, as elucidated in section 2.3.2), and from the Pb $6s^2$ lone pair [9, 10] similar to the case of BiFeO$_3$ (section 4.1).

From the high-temperature paraelectric cubic phase, there are six equivalent $\langle 001 \rangle$ directions for the polar distortion of the central Pb atom, giving rise to six possible domain orientations separated by either 180° or 90° domain walls, illustrated in figure 5.1. 180° domain walls do not introduce any strain into the material, and is not associated with a change in crystallographic orientation. Thus, for techniques not measuring the direction of the polarization directly, 180° domain walls are difficult to detect and, as for TEM, the only difference between the two domains is a phase difference as the electron beam passes through one domain or the other. Thus, only techniques employing phase information, such as certain diffraction or holography methods, can be applied to distinguish 180° domains. 90° domains, on the other hand, are more easily distinguished as they lead to a change in the crystallographic orientation of the material, manifested for example in selected area diffraction patterns of the two domains.

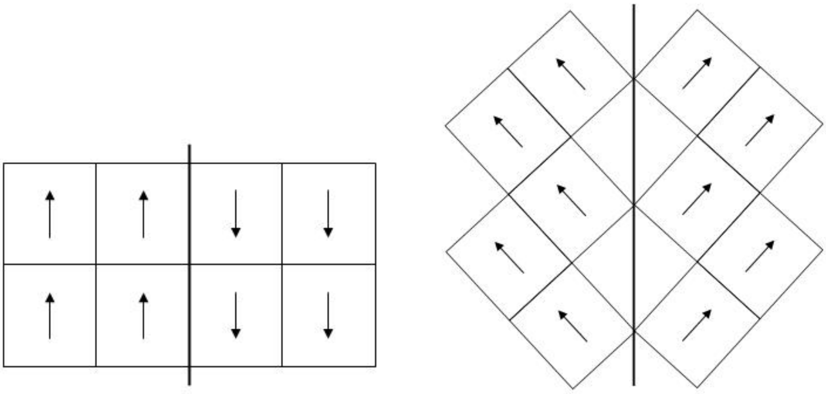
(a) (b)

Figure 5.1: *Simplified schematic drawing of (a) 180° ferroelectric domain wall along [001] and (b) 90° ferroelectric domain wall along [101].*

In bulk, the domain pattern of lead titanate has shown a lamellar structure with both 180° and 90° domains present [11, 12, 13]. As dimensions and length scales are reduced, the collective long-range nature of ferroelectricity sets in to respond to the change in boundary conditions. Of the reduced dimensionality ferroelectric structures, two-dimensional (2D) thin films are the far most studied. The domain structures of these show a dependence on strain to the substrate, electric boundary conditions and film thickness [2]. It is reasonable to believe that synthesis parameters along with surface and size effects will influence the domain structure also in the case of one-dimensional (1D) ferroelectrics. Although few reports have emerged on 1D lead titanate so far, experimental reports on other ferroelectric perovskites have not pointed to a "universal" 1D domain structure [14, 15, 16, 17].

One of the critical issues of ferroelectric memory devices is the fatigue of the material, a decrease in the ability to switch between ferroelectric (preferably 180°) domain states after repeated switching. This fatigue can be related to a number of mechanisms such as pinning of domain walls to defects or inhibition of nucleation of the preferred domain [18]. Another application issue is imprinting, or the preference of one domain orientation over the other. All of these mechanisms are strongly related to defects in the crystal [18, 19]. It is thus of critical importance to know the structure of ferroelectrics down to an atomic level.

5.2 *Paper 4:* Polarization control in ferroelectric PbTiO$_3$ nanorods

Paper 4 has been submitted to *Journal of Applied Physics* and is a continuation of previously published work [20, 21, 22].

It is a combined TEM and piezoelectric force spectroscopy (PFS) study of lead titanate nanorods hydrothermally synthesized [21, 22] at a temperature of 180 °C, below the Curie temperature T_C. The earlier TEM studies showed that the formation mechanism is self assembly of ~10 nm sized lead titanate nanocubes, probably aligned by their inherent polarization to form long (about 1 μm) nanorods growing from bur-like structures. The TEM studies reported here are mainly on nanorods heat treated to 600 °C, above T_C.

The main conclusion is that a flipping of the ferroelectric axis of the nanorods from axially to radially occurs upon heat-treatment. Further, upon heat-treatment, 90° domains are introduced in the nanorods in a fashion neither found experimentally in other 1D ferroelectrics nor earlier predicted theoretically. Both the experimental TEM work and the interpretation of the data presented in this article are my own work, while PFS measurements and interpretation were performed primarily by Per Martin Rørvik.

Polarization control in ferroelectric $PbTiO_3$ nanorods

Ragnhild Sæterli,[1] Per Martin Rørvik,[2] Chang Chuan You,[3] Randi Holmestad,[1] Thomas Tybell,[3] Tor Grande,[2] Antonius T. J. van Helvoort,[1] and Mari-Ann Einarsrud[2,]*

[1]Department of Physics, Norwegian University of Science and Technology, 7491 Trondheim, Norway

[2]Department of Materials Science and Engineering, Norwegian University of Science and Technology, 7491 Trondheim, Norway

[3]Department of Electronics and Telecommunications, Norwegian University of Science and Technology, 7491 Trondheim, Norway

* To whom correspondence should be addressed:
Professor Mari-Ann Einarsrud
Department of Materials Science and Engineering
Norwegian University of Science and Technology
7491 Trondheim
Norway
E-mail: mari-ann.einarsrud@material.ntnu.no
Telephone: +47 73594002

Abstract

We demonstrate by transmission electron microscopy and piezoresponse force spectroscopy that the polarization direction in hydrothermally synthesized lead titanate ($PbTiO_3$) nanorods can be changed from parallel to the nanorod axis to perpendicular to it by a simple heat treatment above the Curie temperature. The heat treatment also caused a rearrangement of the surface and a reduction in the amounts of defects. The polarization of the heat-treated nanorods could be successively switched in the direction perpendicular to the nanorod axis. This control of the polarization in $PbTiO_3$ nanorods opens up possibilities of tailoring the ferroelectric properties and is therefore highly relevant for the use of ferroelectric nanorods in devices.

I. INTRODUCTION

Ferroelectric nanostructures are important in various applications such as non-volatile ferroelectric random access memory, nanoelectromechanical systems, nanoscale capacitors, advanced sensors, energy-harvesting devices and in photocatalysis.[1,2] Lead titanate (PbTiO$_3$) is a prototype displacive ferroelectric material with a Curie temperature (T_C) of 490 °C and a high spontaneous polarization of 75 $\mu C/cm^2$.[2] PbTiO$_3$ has a tetragonal perovskite structure with lattice parameters a = 3.90 Å and c = 4.15 Å. The study of nanoscale properties of PbTiO$_3$, such as the critical size for ferroelectricity, has mainly been concentrated on zero-dimensional nanoparticles and islands[3-6] and two-dimensional thin films,[7-10] while investigations of ferroelectricity in one-dimensional (1D) PbTiO$_3$ nanostructures, such as nanorods, nanowires and nanotubes, are scarce. The main reason is the challenge of preparing high-quality 1D nanostructures of PbTiO$_3$, especially single-crystalline nanostructures, which are the most interesting for applications as well as for fundamental studies of ferroelectricity. Recently, low-temperature hydrothermal methods, where the synthesis takes place far below T_C, have proven successful in producing single-crystalline PbTiO$_3$ nanowires and nanorods.[11-13] In the lack of experimental evidence various theoretical studies have shed light on the ferroelectricity in 1D ferroelectric nanostructures.[14-16]

For using ferroelectric nanorods in device applications it is important to be able to control the polarization direction and the domain structure. For instance, for nanorods in energy-harvesting devices the polarization is probably best oriented along the axis to take advantage of the higher volume contraction or extension, while for nanorods in memory applications the polarization may be better oriented perpendicular to the axis to increase the bit density. Domain structures are formed as a consequence of minimizing the elastic and electrostatic energy of a ferroelectric system and have a profound influence on the physical properties of ferroelectrics. Hence it is of interest to investigate how the domain structure and the polarization direction of ferroelectric nanorods can be controlled and optimized for a given device application.

Most studies on nanorods and nanowires of ferroelectric perovskites report that the polarization is oriented along the nanorod axis, but there exist some studies which show results indicating that the polarization can at least partially be perpendicular to the axis in nanorods/nanowires of $BaTiO_3$ and $PbZr_{1-x}Ti_xO_3$ (PZT).[17-24] Wang *et al.* observed domain walls oriented ~45° to the nanorod axis in PZT nanowires that were made by hydrothermal synthesis followed by annealing.[22,23] This corresponds to a domain structure with the polarization alternating along and perpendicular to the nanorod axis. Such a domain structure was also observed by Schilling *et al.* in $BaTiO_3$ nanocolumns that were fabricated by focused ion beam cutting of $BaTiO_3$ single crystals.[24]

Our previous work has shown that hydrothermally synthesized $PbTiO_3$ nanorods are oriented with the [001] direction or c-axis of the tetragonal perovskite structure along the nanorod axis.[12,13,25] The nanorods are grown directly in the tetragonal state at 180 °C, far below the T_C. Here, we report control of the polarization direction and domain structure in $PbTiO_3$ nanorods by annealing. By a combination of transmission electron microscopy (TEM) and piezoresponse force spectroscopy (PFS) we show that the stable polarization direction can be tuned from parallel to perpendicular to the nanorod axis by heat treatment above T_C, while at the same time improving the crystal quality.

II. EXPERIMENTAL DETAILS

A. Synthesis

The $PbTiO_3$ nanorods were synthesized by a hydrothermal method as previously reported.[12,13] Briefly, an amorphous $PbTiO_3$ precursor (10 mmol) was hydrothermally treated at 180 °C for 48 h in the presence of a surfactant (sodium dodecylbenzenesulfonate). The dispersion volume was 50 mL and the surfactant/Pb molar ratio was 1.5:1. The product was washed in distilled water and ethanol and dried at 100 °C.

To study the effect of heat treatment in air, some of the nanorods were studied untreated, some were heat-treated at 350 °C (below T_C) and some at 600 °C (above T_C) for 6 h. The heating and cooling rates were 200 °C/h. Not heat-treated nanorods are addressed as “as-grown”, those heat-treated at 600 °C as “heat-treated”, while those heat-treated at 350 °C will be addressed as such.

B. TEM characterization

Specimens for TEM were prepared by two different procedures. First, conventional TEM specimens were made by dispersing and crushing the synthesis product in ethanol, and subsequently dripping the dispersion on to a TEM copper grid covered by an amorphous electron transparent holey carbon foil. In this way, the nanorods lie flat on the carbon foil and a sideways view (perpendicular to the nanorod axis) of the nanorods is obtained.

Cross-sectional TEM specimens of the nanorods were obtained by embedding the powder in epoxy before microtoming into electron transparent slices (~50-100 nm). This method gives fragments of the rods in random orientations. Here we focus on nanorods that were cut close to perpendicular to the nanorod axis, enabling a cross-section edge-on view of the nanorods by proper orientation of the TEM specimen. The combination of conventional and cross-section TEM specimens allows a three-dimensional understanding of the nanorod morphology and domain structure.

The as-grown and the heat-treated nanorods were prepared by each of the two TEM specimen preparation methods and investigated using selected area electron diffraction (SAED) and TEM imaging techniques. For this, a 200 kV field-emission JEOL 2010F microscope was used. Details on the characterization of the as-grown nanorods have been described elsewhere.[25]

C. PFS measurements

Piezoresponse hysteresis loops were obtained by piezoresponse force spectroscopy. Individual $PbTiO_3$ nanorods were dispersed onto a gold film on a silicon substrate and studied by PFS in vertical and lateral mode using a Veeco Multimode V atomic force microscope (AFM) equipped with a NanoScope V controller and a signal access module. Platinum/iridium-coated Veeco SCM-PIT probes with nominal force constant 2.8 N/m were used. Prior to the PFS study, the samples were studied with field-emission scanning electron microscopy (FESEM, Zeiss Ultra 55, used at 5 kV) to locate individual nanorods that could be used in the PFS study. Such nanorods were lying flat on the substrate, had no particles or other nanorods nearby, and had a relatively consistent diameter throughout the length. The torsional force afflicted onto the tip in lateral PFS mode along the nanorod axis was maximized by aligning the samples such that the nanorod axis was perpendicular to the AFM cantilever length direction.

The surface of the sample with dispersed nanorods was examined in AFM tapping mode to locate the preselected nanorods. For the PFS measurements, the tip was placed at a desired spot on the nanorod in contact mode with zero scan size. Measurements were performed along the nanorods at several spots while sweeping the dc bias between -10 V and +10 V, using an ac bias with amplitude of 1 - 5 V and a frequency of typically 3 kHz. The PFS amplitude and phase signals were detected through an external lock-in amplifier (Stanford Research Systems SR830 DSP). The dc bias sweep time was 100 s for one cycle with a number of 256 data points. After the PFS study, the nanorods were re-examined by AFM in tapping mode and FESEM to verify that the nanorods had not been displaced or damaged during the PFS measurements.

III. RESULTS

Figure 1(a) shows a typical bright field TEM image from the as-grown, dispersed specimen. The nanorods are single-crystalline, and are generally several hundred nm long with widths of 30-100 nm. A SAED pattern of a typical as-grown nanorod is shown in Fig. 1(b), revealing that the $PbTiO_3$ [001] c-axis is parallel to the nanorod axis for as-grown nanorods, hence they have the polarization parallel to the elongated axis of the nanorods. TEM examination of nanorods heat-treated to 350 °C (not shown) gave results consistent to those of the as-grown nanorods.

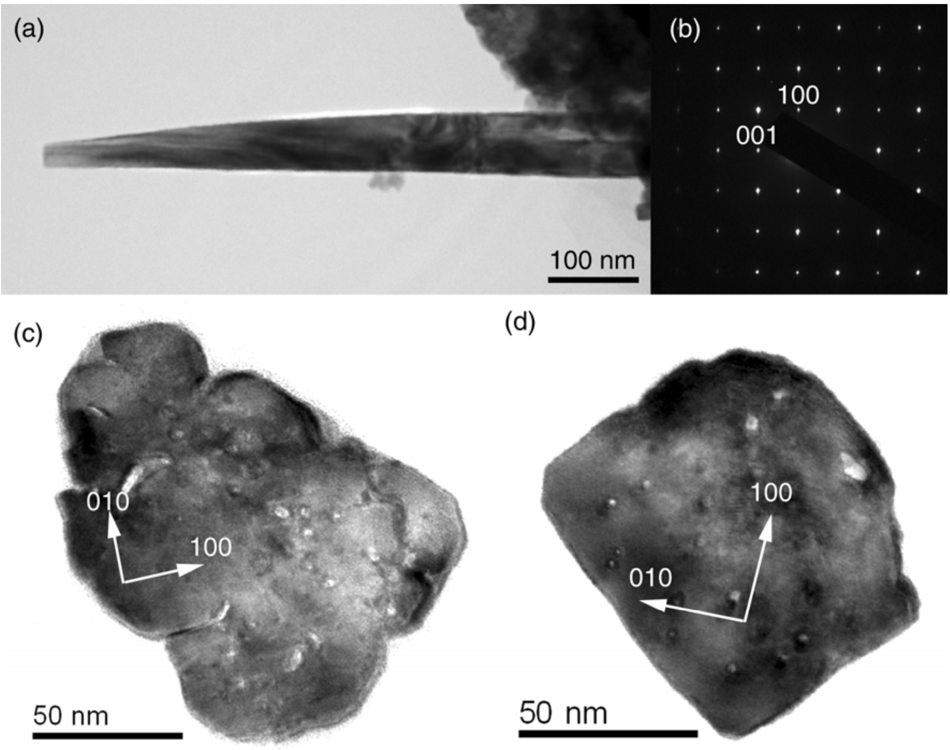

Figure 1. (a) Representative TEM image of an as-grown nanorod prepared by a conventional TEM specimen preparation method. (b) SAED pattern from the [010] zone axis of the nanorod in (a), revealing a nanorod axis of [001]. (c), (d) TEM images of as-grown nanorods viewed along the nanorod axis, prepared by microtomy.

To study the morphology of the nanorods in more detail, cross-section specimens were prepared. Two typical cross-sections of as-grown nanorods are shown in Fig. 1(c)-(d). The outer shape of the nanorod cross-sections is highly irregular, with mainly {100} or {110} surfaces. In addition, notches in the surface and voids in the inner part of the nanorods are present. These observations are further elucidated by Sæterli *et al.*[25]

Upon heat treatment above T_C, the polar [001] direction rotated 90° and became perpendicular to the nanorod axis. This change is evidenced by the image and the corresponding SAED pattern shown in Fig. 2(a)-(b). The SAED pattern also shows splitting of the diffraction peaks typical of 90° domains. Representative examples of cross-sectional specimens of the heat-treated nanorods are shown in Fig. 2(c)-(d). The heat-treated nanorods were comparably more homogeneous and contained fewer defects than the as-grown nanorods. Also, the shapes were more rectangular with mainly {100} or {001} surface planes, having {101} surfaces at the truncated corners. The dominance of {110} surface planes typically observed in the as-grown nanorods (Fig. 1(c)-(d)) was not observed in the heat-treated nanorods.

The cross-section analysis of the heat-treated nanorods also revealed 90° domain walls, as indicated by red arrows in Fig. 2(c)-(d). A high resolution image of the domain wall indicated in Fig. 2(c) is shown in Fig. 3(a), while a SAED pattern of the whole cross-section is given in Fig. 3(b). The splitting of the diffraction peaks in Fig. 3(b) clearly indicates two domains in the cross-section separated by a 90° domain wall. Typically one to three domains, having parallel domain walls along {101} planes, were found on a nanorod cross-section. It is important to note that the domain walls tend to end in the middle of a {100}/{001} surface, rather than at a corner or notch. For comparison, a high resolution image and SAED pattern of the as-grown nanorod cross-section from Fig. 1(c) are shown in Fig. 3(c)-(d).

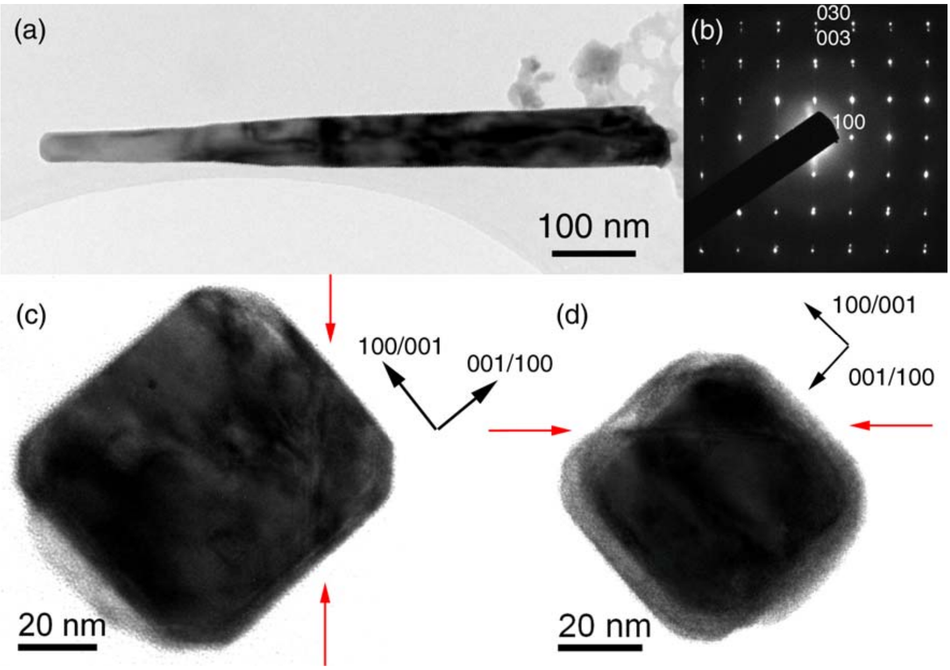

Figure 2. (a) Representative TEM image of a heat-treated nanorod prepared by a conventional TEM specimen preparation method. (b) SAED pattern from the [001]/[010] zone axis of the nanorod, indicating a nanorod axis of [100]. The splitting of the diffraction peaks indicates 90° domains with the [001] direction oriented perpendicular to the nanorod axis. (c), (d) TEM images of heat-treated nanorods viewed along the nanorod axis, prepared by microtomy. Surface planes are on {100} and {001} planes for the long sides and on {101} planes for the truncated corners. 90° domain walls are found on {101} planes and are indicated by red arrows.

Initial PFS measurements on as-grown nanorods, and on nanorods heat-treated at 350 °C, were inconclusive with regard to the crystallographic orientation as no apparent hysteresis loops were obtained, possibly a result of low piezoelectric activity in the lateral direction as well as remaining defects and inhomogeneities in the nanorods after synthesis.[12,13,25]

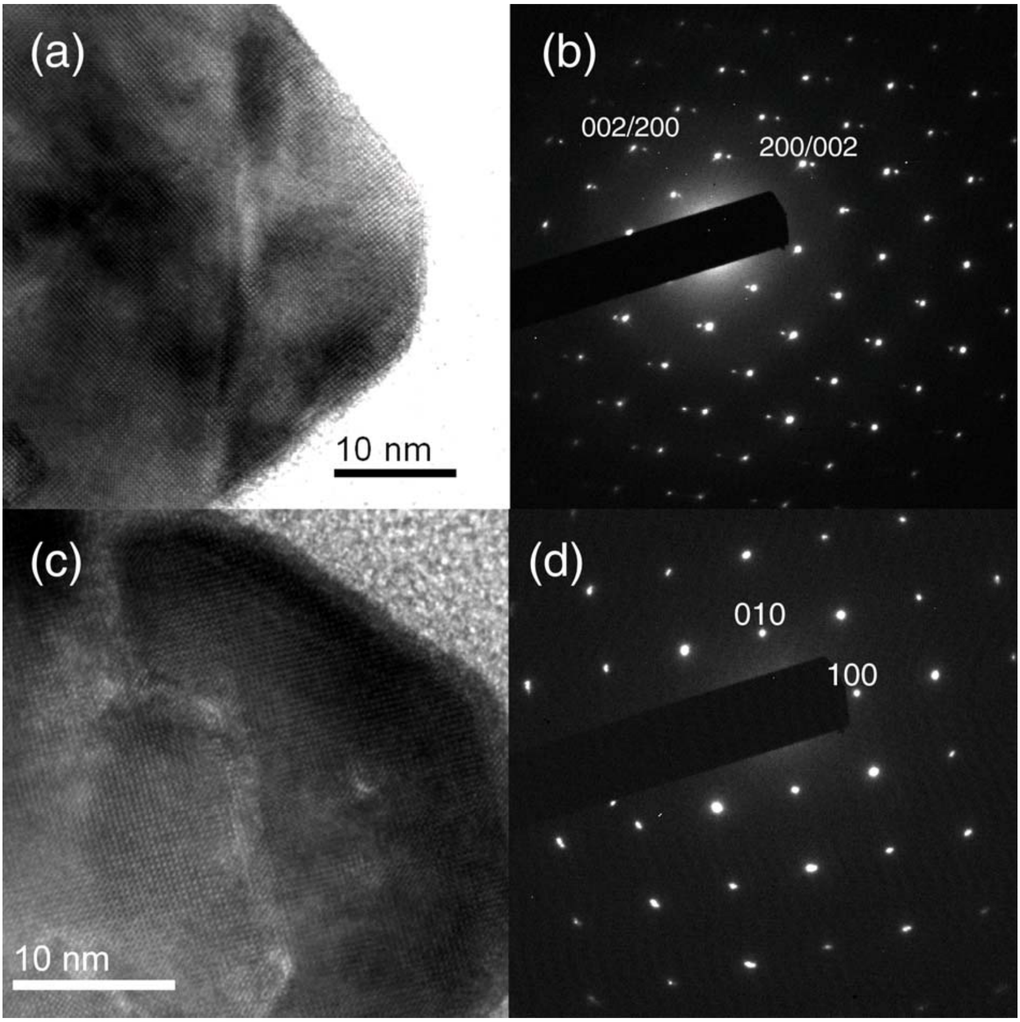

Figure 3. (a) High resolution TEM image of the heat-treated nanorod cross-section from Fig. 2(c), showing the 90° domain wall. (b) SAED pattern of the cross-section in (a), showing the splitting of diffraction peaks due to the two domains. (c) High resolution TEM image of the as-grown nanorod cross-section in Fig. 1(c), showing scattered defects and voids in the crystal. (d) SAED pattern of the cross-section in (c), showing the single-crystallinity of the nanorod.

Figure 4(a) shows a FESEM image of a heat-treated nanorod on the gold film. The output amplitude and phase signals from the PFS study of this nanorod using an ac bias amplitude of 1 V is shown in Fig. 4(b)-(e), both in the vertical (perpendicular to the nanorod axis) and lateral (parallel to the nanorod axis) directions of the nanorod. In

Fig. 5, the measured piezoresponse $P = A \times \cos$ in the vertical direction calculated from the amplitude (*A*) and phase ( ) signals in Fig. 4(b)-(c) are shown as hysteresis 1. The evident vertical piezoresponse and lack of clear lateral piezoresponse support the TEM observation of polarization direction perpendicular to the nanorod axis. Measurements from other points on the nanorod showed similar responses.

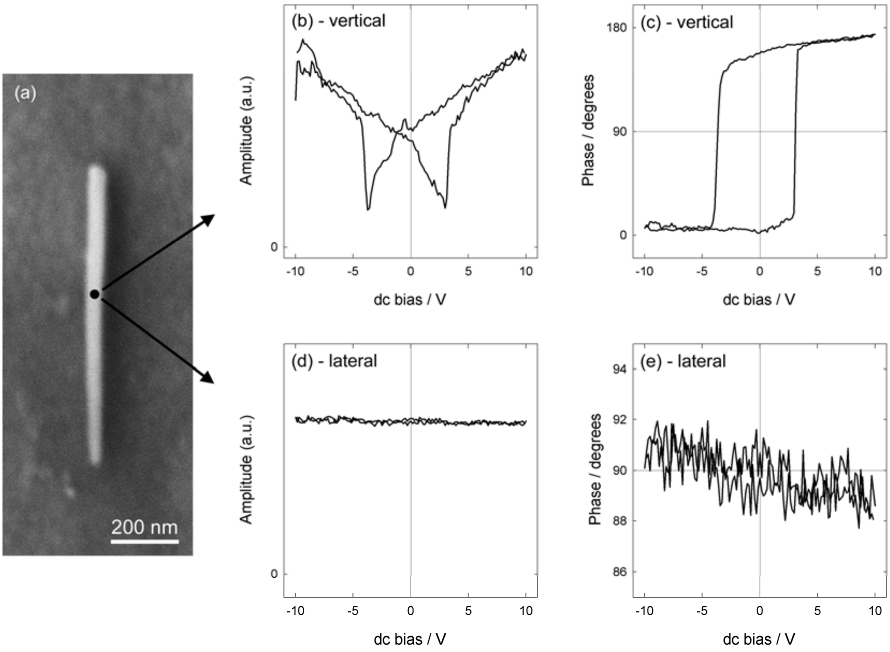

Figure 4. FESEM image and PFS study of a $PbTiO_3$ nanorod heat-treated at 600 °C. (a) FESEM image taken before the PFS study. (b) Amplitude signal and (c) phase signal in the vertical direction. (d) Amplitude signal and (e) phase signal in the lateral direction. The measurements were performed on the indicated spot on the nanorod. The ac bias amplitude was 1 V for both measurements.

To verify that the out-of-plane polarization could be consecutively switched in the vertical direction, several PFS measurements were performed in succession on a chosen spot of the nanorod (Fig. 5). The hysteresis loops of the piezoresponse have a similar width, implying a constant coercive field. The amplitude of the piezoresponse was reduced slightly with repeated measurement. Multiple repeated PFS measurements on one spot of a nanorod often induced decomposition of the nanorod and/or accumulation of nanoparticles onto the nanorod, observed by AFM topography imaging and FESEM after PFS measurements, especially if a high ac bias amplitude (5 V) was used in the PFS measurements.

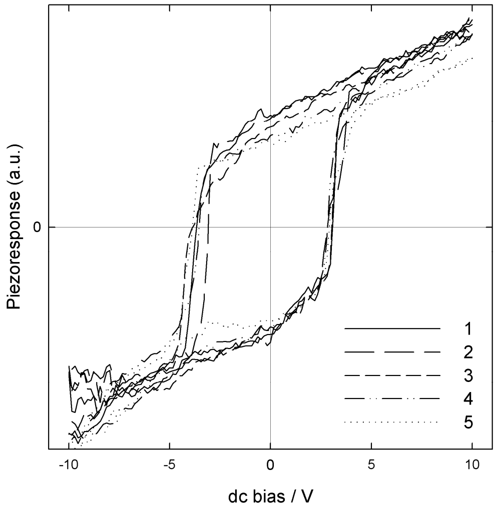

Figure 5. Piezoresponse in the vertical direction of the nanorod in Fig. 4(a) measured five times in succession. All measurements were performed on the same spot on the nanorod, with 1 V ac bias amplitude. Hysteresis 1 is calculated from the amplitude and phase signals in Fig. 4(b) and (c), respectively.

IV. DISCUSSION

The exact domain structure is an important factor for device applications. In bulk $PbTiO_3$ both 90° and 180° domain walls have been shown to be present,[26,27] while the domain structure in epitaxial thin films depends on the misfit strain between the substrate and the film, the thickness, and the electrostatic environment.[7] In ferroelectrics, domain walls, and domains, are typically introduced to minimize the depolarization energy. However, the presence of free charges, both volume charges and at surfaces, and imperfections will influence the final domain state. The as-grown $PbTiO_3$ nanorods studied here did not show any sign of domain structure, although the presence of 180° domains cannot be excluded on the basis of our TEM and PFS experiments. Both the TEM and the PFS results show that the polarization direction in the heat-treated PbTiO$_3$ nanorods is perpendicular to the nanorod axis, unlike the as-grown nanorods in which the polarization direction is parallel to the axis. The heat treatment above T_C thus causes a change in the polarization direction and the domain structure of the nanorods. Some studies indicate that the polarization can be perpendicular to the axis in nanorods/nanowires of other ferroelectric perovskites,[17-24] however to the best of our knowledge this is the first report in the case of PbTiO$_3$ nanorods. Moreover, the annealing above T_C resulted in nanorods having less defects.

One important difference between the as-grown and the heat-treated rods is that the as-grown rods are ferroelectric during growth, whilst the heat-treated rods go through a cubic to tetragonal phase transition during cooling. The synthesis temperature of 180 °C is far below the T_C of PbTiO$_3$, so the nanorods grow in the tetragonal phase. In other studies it has been demonstrated that single-domain PbTiO$_3$ structures, such as 1.2   m thick films[28] and platelike nanoparticles,[29] also can be grown by hydrothermal synthesis. Hence, the axial polarization direction, and lack of domain structure, in the as-grown nanorods is not due to the thermodynamic phase transition, but rather due to the synthesis conditions and the formation process of these nanorods. The rods are formed by self-assembly of cube-shaped or facetted nanoparticles with a size in the order of 10 nm,[12,13] and we suggest that the mechanism by which this self-assembly is conducted is related to the direction of polarization. In addition, the highly alkaline environment necessary for hydrothermal synthesis of PbTiO$_3$ has a high concentration of ions and surfactants that can adsorb on the surfaces of the growing nanostructures. Thus, the single-domain structure observed in these nanorods is probably not the minimum energy configuration for the nanorods.

Our results from the heat-treated nanorods clearly show that the preferred configuration is the one in which the polarization lies perpendicular to the axis, with 90° domain walls introduced along the nanorod axis. The cooling rate of the heat treatment of the nanorods, 200 °C/h, is believed slow enough for the system to reach an equilibrium domain structure. A transition from a polarization along the nanorod axis to a domain state having the polarization perpendicular to the nanorod axis has been predicted theoretically to occur for sufficiently large screening present for very thin nanorods.[30] The size of the nanorods investigated here are relatively large, and upon heating through T_C, adsorbed surfactant molecules will decompose or burn off and the number of defects such as vacancies and incorporated protons (hydroxyl defects) will be reduced.[19,31] Hence, we do not ascribe the stable domain state in the heat-treated nanorods having the polarization perpendicular to the growth direction to a depolarization screening induced phase transition.

We find that the domain configuration in the heat-treated nanorods differ from the situation found in ion beam structured $BaTiO_3$ columns[24] and chemically synthesized PZT nanowires,[22,23] where 90° domains are found, but with domain walls oriented 45° to the axis such that the polarization alternates along and perpendicular to the column/nanowire axis. The SAED pattern in Fig. 2(b), taken from a substantial part of the nanorod length, clearly shows that only one lattice spacing (the a-lattice parameter) is present along the length of the nanorod. In all studied cross-sections of heat-treated nanorods this was confirmed as the c-axis was oriented in the cross-section plane. Furthermore, our results indicate that the 90° domain walls are parallel to the nanorod axis, on {101} planes.

The rearrangement of the surface of the nanorods from {110} planes to primarily {100} and {001} planes upon heat treatment is interesting, since this reconstruction requires substantial mass transport or diffusion. The tendency to form {100} surfaces was also found by Ye *et al.*[29] in their study of $PbTiO_3$ nanoparticles; however, truncation of the corners by {101} planes were not reported. Calculations show that the pseudocubic {100} planes in $PbTiO_3$ are lower in energy than the pseudocubic {110} planes.[32] The surface rearrangement is therefore attributed to minimization of the surface energy. In this picture the increased energy of the {101} surfaces at the truncated corners is thought compensated by a total decrease in energy due to a reduced total surface area. Estimates show that if the difference between the {100} and {110} surface energies is sufficiently small (slightly smaller than the values of the ideal surfaces of Eglitis and Vanderbilt[32]), such a truncation is energetically favourable.

The domain configuration of the heat-treated nanorods, having polarization perpendicular to the nanorod axis, can be due to a competition between depolarization energy and energy gain due to a crystalline arrangement with lowest energy surfaces. Since almost all the domain walls studied have been found to end on {100} or {001} surfaces rather than on corners or notches, it is likely that surface pinning does not plays a major part in their placement. Thus, the domain walls are present in order to minimize the depolarization energy and hence help stabilize the perpendicular domain configuration. We also note that the domain configuration can be influenced by the presence of free charges that are readily available under atmospheric conditions.[18]

The presented data emphasizes the importance of correct surfaces in order to control the domain configuration having a polarization perpendicular to the nanorod axis. For any further study of the connection between domain configuration and surfaces, it would be interesting to see calculations on the energy differences between the tetragonal {100} and {001} planes, {110} and {101} planes etc., but no such calculations have been performed to the authors' knowledge.

Based on this study, PbTiO$_3$ nanorods with diameters in the size range studied here should be grown below T_C to have polarization along the axis. Otherwise, the polarization will likely orient perpendicular to the axis during cooling through T_C. The ability to control the polarization direction and surface conditions as well as to reduce the amount of defects can be very important for device applications. We have previously shown how PbTiO$_3$ nanorod arrays can be grown on various substrates and how the growth direction can be controlled.[33,34] By combining this knowledge with the demonstrated control of the polarization direction such nanorods can be used in a variety of applications. The possibility of changing the polarization direction and at the same time increasing the quality of the material by a simple heat treatment procedure is therefore relevant for the future use of ferroelectric nanorods.

V. CONCLUSIONS

The $PbTiO_3$ nanorods in this study were examined both as-grown and after heat treatment above T_C, revealing that the polarization direction changed from along the nanorod axis in the as-grown nanorods to perpendicular to it in the heat-treated nanorods. Upon heat treatment, 90° domains were usually introduced with domain walls along {101} and the surfaces were stabilized on {100} and {001} planes with truncated corners on {101} planes. In addition, the amount of defects was reduced. Piezoresponse was observed perpendicular to the axis of the heat-treated nanorods and it was shown that the polarization could be repeatedly switched. The change of polarization direction upon heat treatment demonstrates the importance of growth environment and temperature in controlling the domain structure of ferroelectric 1D nanostructures. The possibility to tailor the polarization direction by a simple heat treatment is highly relevant for the use of nanorods in device applications as the desired polarization direction depends on the function of the nanorods in the actual device.

ACKNOWLEDGMENTS

This work was financially supported by the Strategic Area of Materials at the Norwegian University of Science and Technology (NTNU), NTNU NanoLab and the Research Council of Norway (NANOMAT, Grants no. 158518/431 and 162874).

REFERENCES

[1] A. Gruverman and A. Kholkin, Rep. Prog. Phys. **69**, 2443 (2006).

[2] K. M. Rabe, M. Dawber, C. Lichtensteiger, C. H. Ahn, and J.-M. Triscone, *Modern Physics of Ferroelectrics: Essential Background*, pp 1-30 in *Physics of Ferroelectrics: A Modern Perspective* (*Topics in Applied Physics* Vol. 105), edited by K. M. Rabe, C. H. Ahn, and J.-M. Triscone (Springer, Berlin/Heidelberg, 2007).

[3] B. Jiang, J. L. Peng, L. A. Bursill, and W. L. Zhong, J. Appl. Phys. **87**, 3462 (2000).

[4] A. Roelofs, T. Schneller, K. Szot, and R. Waser, Nanotechnology **14**, 250 (2003).

[5] E. Erdem, H.-C. Semmelhack, R. Böttcher, H. Rumpf, J. Banys, A. Matthes, H.-J. Gläsel, D. Hirsch, and E. Hartmann, J. Phys.: Condens. Matter **18**, 3861 (2006).

[6] C. C. You, R. Takahashi, A. Borg, J. K. Grepstad, and T. Tybell, Nanotechnology **20**, 255705 (2009).

[7] N. Setter, D. Damjanovich, L. Eng, G. Fox, S. Gevorgian, S. Hong, A. Kingon, H. Kohlstedt, N. Y. Park, G. B. Stephenson, I. Stolichnov, A. K. Taganstev, D. V. Taylor, T. Yamada, and S. Streiffer, J. Appl. Phys. **100**, 051606 (2006).

[8] D. D. Fong, G. B. Stephenson, S. K. Streiffer, J. A. Eastman, O. Auciello, P. H. Fuoss, and C. Thompson, Science **304**, 1650 (2004).

[9] C. Lichtensteiger, J.-M. Triscone, J. Junguera, and P. Ghosez, Phys. Rev. Lett. **94**, 047603 (2005).

[10] A. T. J. van Helvoort, Ø. Dahl, B. G. Soleim, R. Holmestad, and T. Tybell, Appl. Phys. Lett. **86**, 092907 (2005).

[11] Y. Hu, H. Gu, X. Sun, J. You, and J. Wang, Appl. Phys. Lett. **88**, 193120 (2006).

[12] G. Wang, R. Sæterli, P. M. Rørvik, A. van Helvoort, R. Holmestad, T. Grande, and M.-A. Einarsrud, J. Nanosci. Nanotechnol. **7**, 2538 (2007).

[13] G. Wang, R. Sæterli, P. M. Rørvik, A. T. J. van Helvoort, R. Holmestad, T. Grande, and M.-A. Einarsrud, Chem. Mater. **19**, 2213 (2007).

[14] J. Slutsker, A. Artemev, and A. Roytburd, Phys. Rev. Lett. **100**, 087602 (2008).

[15] T. Shimada, S. Tomoda, and T. Kitamura, Phys. Rev. B **79**, 024102 (2009).

[16] M. Q. Cai, Y. Zheng, B. Wang, and G. W. Yang, Appl. Phys. Lett. **95**, 232901 (2009).

[17] W. S. Yun, J. J. Urban, Q. Gu, and H. Park, Nano Lett. **2**, 447 (2002).

[18] J. E. Spanier, A. M. Kolpak, J. J. Urban, I. Grinberg, L. Ouyang, W. S. Yun, A. M. Rappe, and H. Park, Nano Lett. **6**, 735 (2006).

[19] N. Bao, L. Shen, A. Gupta, A. Tatarenko, G. Srinivasan, and K. Yanagisawa, Appl. Phys. Lett. **94**, 253109 (2009).

[20] M. T. Buscaglia, C. Harnagea, M. Dapiaggi, V. Buscaglia, A. Pignolet, and P. Nanni, Chem. Mater. **21**, 5058 (2009).

[21] S. Berweger, C. C. Neacsu, Y. Mao, H. Zhou, S. S. Wong, and M. B. Raschke, Nat. Nanotech. **4**, 496 (2009).

[22] J. Wang, C. S. Sandu, E. Colla, Y. Wang, W. Ma, R. Gysel, H. J. Trodahl, N. Setter, and M. Kuball, Appl. Phys. Lett. **90**, 133107 (2007).

[23] J. Wang, C. S. Sandu, and N. Setter, IEEE T. Ultrason. Ferr. **56**, 1813 (2009).

[24] A. Schilling, R. M. Bowman, G. Catalan, J. F. Scott, and J. M. Gregg, Nano Lett. **7**, 3787 (2007).

[25] R. Sæterli, A. T. J. van Helvoort, G. Wang, P. M. Rørvik, B. S. Tanem, T. Grande, M.-A. Einarsrud, and R. Holmestad, J. Phys.: Conf. Ser. **126**, 012010 (2008).

[26] C. C. Chou and C.-S. Chen, Ceram. Int. **26**, 693 (2000).

[27] C. C. Chou, L. C. Yang, and C. M. Wayman, Mater. Chem. Phys. **36**, 57 (1993).

[28] W. W. Jung, H. C. Lee, W. S. Ahn, S. H. Ahn, and S. K. Choi, Appl. Phys. Lett. **86**, 252901 (2005).

[29] Z. Ye, E. B. Slamovich, and A. H. King, J. Mater. Res. **20**, 558 (2005).

[30] I. Ponomareva, I. Naumov, and L. Bellaiche, Phys. Rev. B **72**, 214118 (2008).

[31] F. F. Lange and G. K. L. Goh, J. Ceram. Proc. Res. **2**, 4 (2001).

[32] R. I. Eglitis and D. Vanderbilt, Phys. Rev. B **76**, 155439 (2007).

[33] P. M. Rørvik, Å. Almli, A. T. J. van Helvoort, R. Holmestad, T. Tybell, T. Grande, and M.-A. Einarsrud, Nanotechnology **19**, 225605 (2008).

[34] P. M. Rørvik, T. Grande, and M.-A. Einarsrud, Cryst. Growth Des. **9**, 1979 (2009).

5.3 Additional results

The use of the microtomy sample preparation technique to obtain cross-sections from nanorods embedded in non-conducting epoxy, as described in paper 4, opens up possibilities for characterization of the nanorods beyond the standard TEM techniques and offers insight not easily obtained otherwise. This section describes two experiments on the nanorod cross-sections, first an attempt to image ferroelectric domains and fields by holography, and second a study to try to shed light on surface effects[1].

5.3.1 Holographic experiments

Electron holography is a technique capable of recording both the amplitude and the phase of the exit wave, in contrast to standard TEM imaging which only detects the amplitude[2]. This opens up possibilities to image *phase objects*, objects and phenomena that give a change in the phase of the electron beam only, such as magnetic and electric fields [23]. It has also potential to increase resolution of the TEM due to correction of objective lens spherical aberrations [24].

Though electron holography has been around for quite a while[3], the need for optimized instrumentation is probably one of the major issues that has prevented it from becoming a universal TEM technique. Its usefulness to both basic and applied research should be beyond doubt, with reports from such diversified fields as imaging viruses in life sciences [26], detection of dopant profiles in semiconductor industry [27] and magnetization of nanoparticles in solid state physics [28, 29]. A few applications to ferroelectrics have also been reported [30, 31], however in far less numbers than for magnetic systems.

The basic principle of electron holography is that a reference beam is allowed to interfere with the beam transmitted through the object, and the resulting interference pattern is recorded. Subsequent image processing is then required to obtain either the amplitude or the phase image, recon-

---

[1] "Surface effects" taken here to mean the outermost nanometers of the material, rather than Å as in surface science.

[2] Although the phase of the object does contribute to various TEM techniques such as high resolution imaging, it does so by influencing the *amplitude* of the exit wave.

[3] The electron holography technique was invented already in the 1940s by D. Gabor [25].

structing the initial object using a reference image which includes details also on microscope parameters such as aberrations.

The reference beam is created by employing a biprism, a biased wire that works effectively as a beam splitter by bending the electron beam on either side to create two virtual electron sources, as illustrated in figure 5.2. This holographic setup is termed "off-axis" due to the different angles of the two beams, and has the advantage that the two can be easily separated in reciprocal space. Obviously, for interference to occur, there is a need for the electron source to be highly coherent, as discussed in [32]. Further, a stigmatism is introduced to the condenser lens to elongate the beam so that nearly parallel coherence fringes are observed.

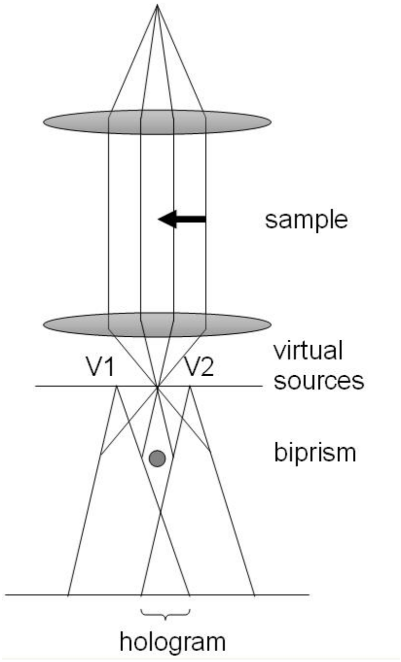

Figure 5.2: *Schematic principle of off-axis electron holograpy.*

Any intrinsic electric field in a material will be observed by holography as a gradual change in phase [30], with the gradient of the phase change being

$$\nabla\phi = \sigma \frac{P}{\epsilon_0(\epsilon_r - 1)} t. \tag{5.1}$$

Here, ϵ_0 and ϵ_r are the dielectric constant and the relative dielectric constant of the sample, respectively, P is the polarization, t the thickness of the sample and σ is an interaction constant given as

$$\sigma = \frac{\pi(1+\frac{eV_0}{m_0c^2})}{\lambda_{wl}V_0(1+\frac{eV_0}{2m_0c^2})}, \tag{5.2}$$

with λ_{wl}, e, V_0 and m_0c^2 being the wave length, charge, acceleration voltage and rest energy of the electrons, respectively. It should be noted that only the component of the polarization that is oriented perpendicular to the electron beam will contribute to this phase shift [31]. Experimentally, the perhaps most challenging part is to avoid any strong amplitude contrast conditions such as thickness variations and defects, which may also cause a change in phase.

The holographs presented here were recorded by Takeshi Kasama at DTU, Denmark, using a Titan Analytical TEM operated at 300kV with a biprism installed. A total of six cross sections from the heat treated lead titanate nanorod sample were investigated, of which two representative ones are reported here. Orientations close to the [010] zone axis were used, selected from the condition that as little diffraction contrast as possible should contribute to the image. This way, the polarization is nearly perpendicular to the electron beam so as to maximize the phase shift. Also thickness maps of the rods are shown to establish the effect of possible thickness changes throughout the cross-sections. These were recorded using unfiltered and zero-loss filtered images and performing the operation

$$t/\lambda = ln(I_u/I_0), \tag{5.3}$$

in each pixel, I_u and I_0 being the intensities of the unfiltered and zero-loss filtered images, respectively.

From equation 5.1, and assuming values of 0.75 C/m^2 and 100 for P and (ϵ_r-1), respectively [33, 34], it is found that for a sample thickness of 50 nm the phase gradient equals $2\pi/23$ rad/nm at 300 kV. In other words, a phase shift of 2π is expected over an area of 23 nm from the edge of the specimen, a small enough area to justify trying the experiment on cross-sections of 20-100 nm width. At thicker specimens, the phase gradient is even larger.

One of the examined cross-sections is shown in figure 5.3(a), with the corresponding selected area diffraction (SAD) pattern shown in figure 5.3(b). The splitting of the peaks comes from the 90° domains, with the characteristic splitting angle of 3.6° due to the tetragonality. A high resolution (HR) image is shown in figure 5.3(c), with the domain wall pointed out in white

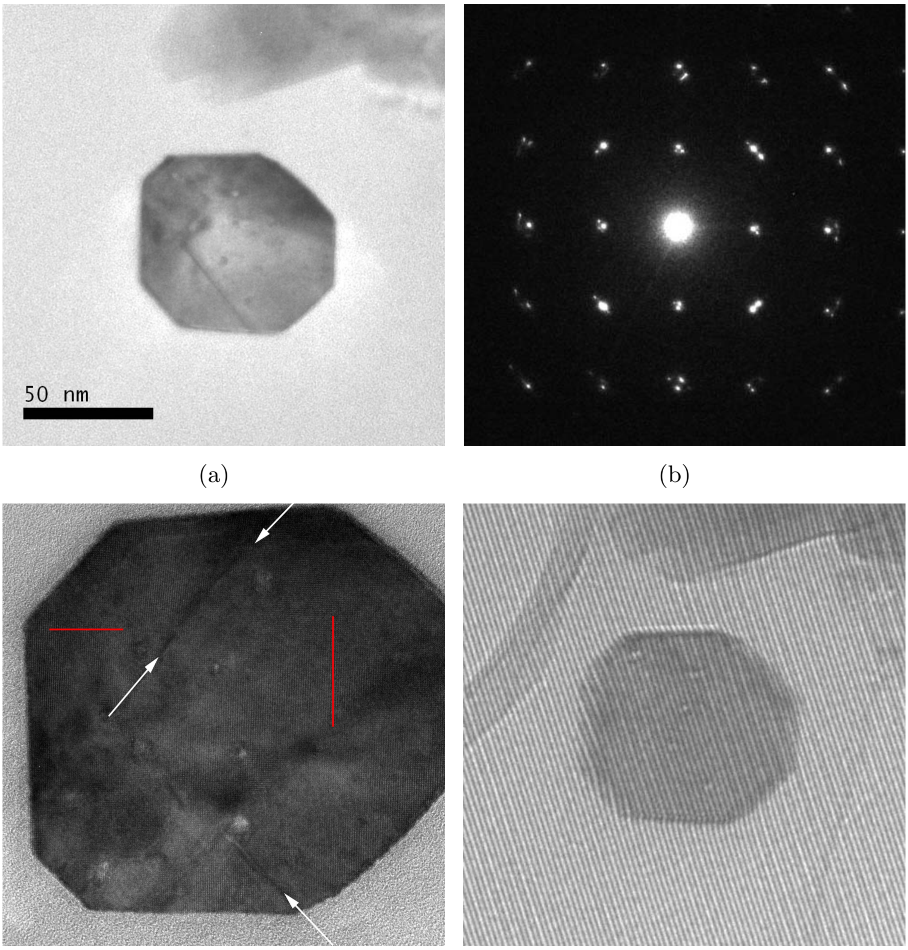

(a) (b)

(c) (d)

Figure 5.3: *(a) TEM image, (b) SAD pattern from a [100] zone axis, (c) HR image and (d) hologram of cross-section of heat treated lead titanate nanorod. The white arrows in (c) show the placement of a 90° domain wall, while the direction of polarization within each domain depicted by a red bar.*

arrows and the direction of polarization within each domain depicted by a red bar. Finally, the recorded hologram is shown in figure 5.3(d).

The reconstructed amplitude and phase maps are shown in figure 5.4, together with a thickness map. No discernible features are found either in the thickness map or in the amplitude map so that any phase difference due to the polarization should indeed be visible in the phase map. The phase map does not, however, show any clear sign of polarization in either of the domains of the cross-section.

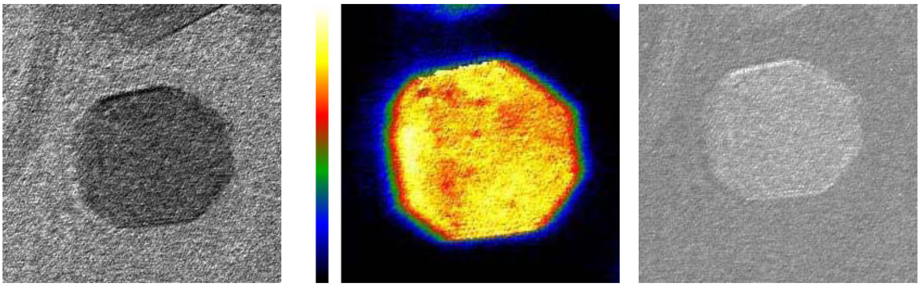
(a) (b) (c)

Figure 5.4: *(a) Amplitude map, (b) phase map and (c) thickness map of the nanorod cross-section in figure 5.3. In (b), black denotes zero phase shift while white denotes a phase shift of 2π, according to the scale bar on the left.*

A hologram of another cross-section is shown in figure 5.5(a), with a domain wall pointed out in white arrows and the direction of polarization within each domain marked with a red bar (found from SAD and HR). Amplitude, phase and thickness maps are shown in figure 5.5(b)-(d), where the color scale in (c) goes from zero phase shift (black) to a phase shift of 3π (white). Again, the thickness and amplitude maps are flat so that any phase shift due to the polarization should be discernible. The phase map does show slight phase variations, however none that is consistently in the direction of polarization (given in figure 5.5(a)).

The reasons why the holographic experiments do not yield any conclusive results, are not clear at the present moment. We do note, however, that the nanorods have quite a few defected areas of pores and lattice imperfections, which can lead to both amplitude contrast and phase contrast potentially masking the effect of polarization or introducing compensating charges into the cross-sections. Also, it is worth noticing that in the similar experiment on barium titanate by Matsumoto *et al.* [30], the authors subtracted the phase change due to the inner potential of the material by also recording holograms above the Curie temperature, a recipe which could prove beneficial also for this experiment.

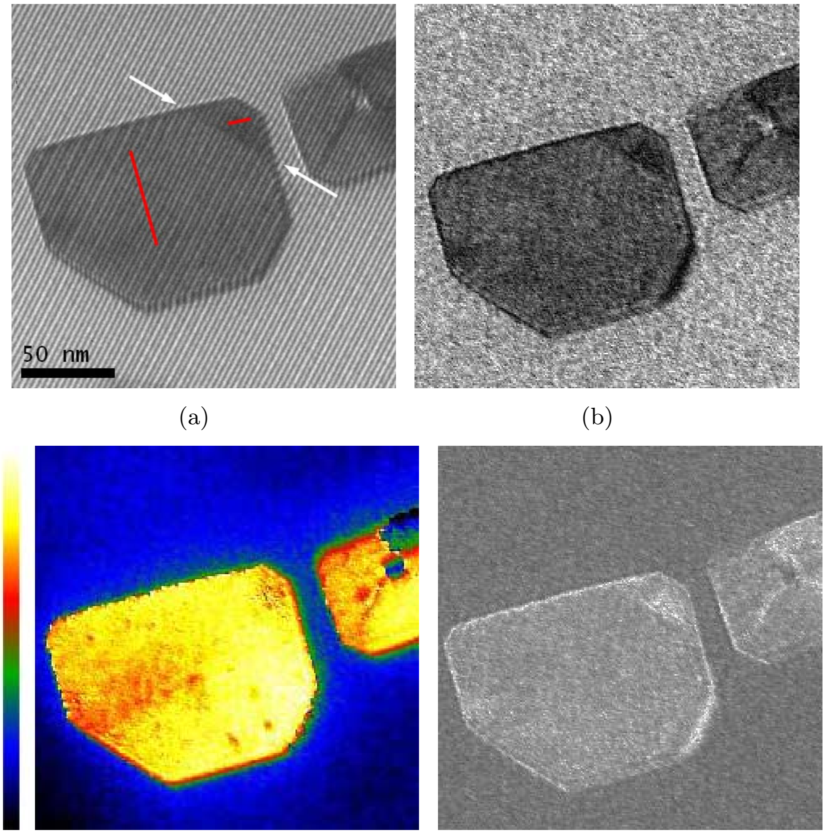

(a) (b)

(c) (d)

Figure 5.5: *(a) Hologram, (b) amplitude map, (c) phase map and (d) thickness map of cross-section of heat treated lead titanate nanorod. The white arrows in (a) show the placement of a 90° domain wall, while the direction of polarization within each domain is depicted by a red bar. The color scale in (c) goes from zero phase shift (black) to a phase shift of 3π (white).*

5.3.2 Surface effects

The cross-sections of heat treated nanorods do, when imaged by Scanning TEM (STEM), show effects unseen in regular TEM imaging. Figure 5.6 shows a high-angle annular dark-field (HAADF) and a low-angle annular dark field (LAADF) STEM image of the same cross-section, revealing a bright band along the edges of the cross-section when imaged using LAADF (collection angle of 17-45 mrad, as compared to >50 mrads in HAADF).

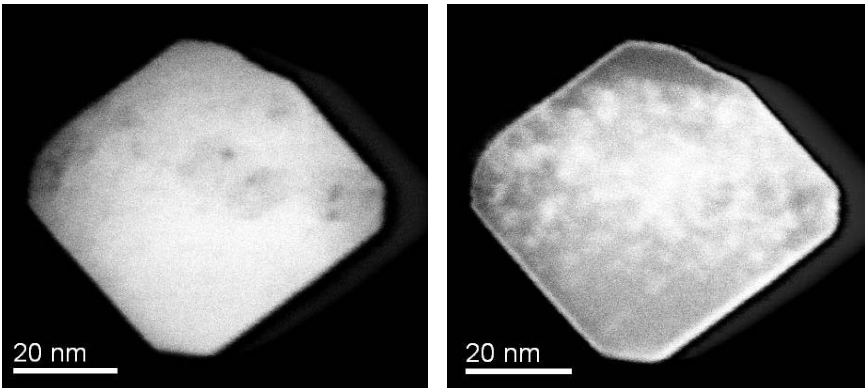

(a) (b)

Figure 5.6: *(a) HAADF STEM (inner collection angle 50 mrad) and (b) LAADF STEM (inner collection angle 17 mrad) image of cross-section of heat treated lead titanate nanorod.*

The annular shape of the STEM detector allows electrons scattered to high angles (compared to those of bright field TEM or SAD diffraction, which are in the order of a few mrads) to be detected without discerning between scattering directions. By scanning a sub-nm sized convergent probe across the specimen, scattered electrons essentially forming an unfiltered CBED pattern are detected. The ability to change the angle of the recorded electrons by changing the camera length of the microscope allows detection of various scattering mechanisms, see, e.g. the review by Liu [35]. One of the great strengths of STEM lies in its capability to form Z-dependent atomic-resolution images (Z = atomic number) without the thickness-focus problem of HR TEM imaging [36]. Still, the perhaps greatest advantage of STEM is the ability to combine a sub-nm (and even sub-Å) probe with techniques such as EELS and EDS [37], even simultaneously as the high-angle scattered electrons are used to form ADF images [38].

To a first approximation the HAADF signal can be treated as incoherent, although the beam itself is highly coherent, due to the detector geometry and phonon scattering [39], with a close to Z^2 dependence on the atomic number. The separation of LAADF and HAADF is somewhat arbitrary, as both ranges detect signals that are composed of large angle elastically scattered electrons, phonon scattered electrons and multiply scattered electrons. The phonon scattering does, however, dominate at larger angles, which is what gives rise to the Z-dependence, while at lower angles, as those used in LAADF, elastically scattered electrons contribute more to the intensity.

In zone-axis orientation, the electron beam sees columns of positively charged atomic cores. The potential inside a crystal is always positive, due to the high energy of the beam electrons, and has its minima centered at the atomic cores. Thus, more electrons are found close to the atomic cores than in the areas between. This effect is known as channeling, and is usually described in terms of Bloch wave theory (see section 2.1.4) [40, 41] although it is equally valid for a (non-periodic) single column of atoms [42]: The electrons traveling close to the atomic column have a bigger chance of getting scattered, and thus give rise to the atomic sensitivity of STEM[4] [45]. The scattering of electrons out of the column is also known as dechanneling.

It has been shown both theoretically and experimentally [46] that for samples of reasonable thicknesses, any strain will introduce itself as increased intensity in LAADF due to dechanneling and thus a re-distribution of the scattering into smaller angles [47]. Thus, while the channeling effect is responsible for the atomic contrast of HAADF, dechanneling due to strain is probably responsible for the increased contrast seen in LAADF in figure 5.6(b).

An attempt to verify the existence and magnitude of this strain has been performed using Geometric Phase Analysis (GPA) [48]. GPA utilizes the Fourier transform of a high resolution image to map out spatial variations of the frequencies in the image, thus obtaining maps of strain, defects or changes in lattice parameters in the image [49, 50]. As changes rather than absolute values are measured, there is a need for a reference area in the image.

Figure 5.7(a) shows a high resolution image of a heat-treated nanorod cross-section, taken on a 2K CCD camera at a JEOL 2010F. Figures 5.7(b)-5.7(d) are strain maps E_{xx}, E_{yy} and E_{xy}, respectively. The strain is defined as

$$Eij = \frac{du_i}{dr_j}, \tag{5.4}$$

u_i being the displacement of lattice fringes and $r_{i,j} = x, y$. x and y follows the [100] and [001] directions nearly horizontally and vertically in the paper plane, respectively. In the strain maps, the black - white scale goes from -0.2 to 0.2 with zero set as the average at a reference area in the upper left hand corner of the images.

---

[4] And also a range of other techniques and phenomena such as ALCHEMI [43], electron energy-loss by channeling electrons [44] and Kikuchi lines [41].

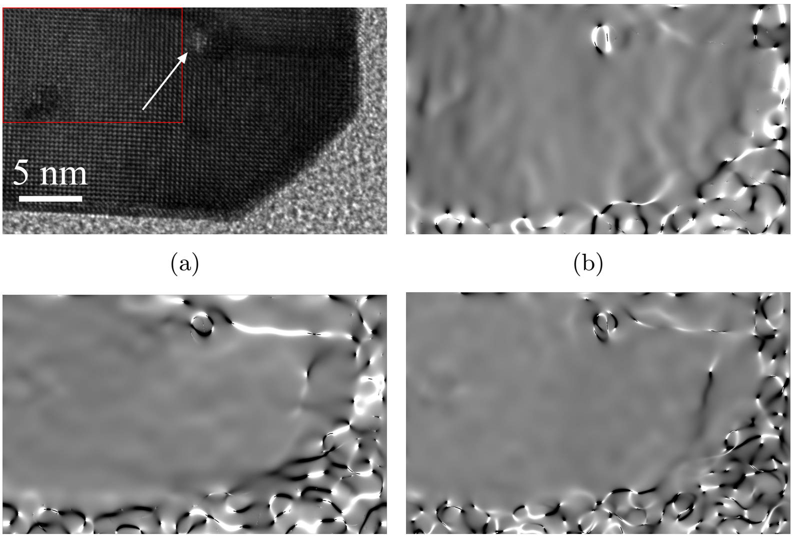

(a) (b)

(c) (d)

Figure 5.7: *(a) High resolution TEM image of part of a heat treated nanorod cross section. A large defect is pointed out with a white arrow, and the reference area is shown by a red box. (b) - (d) Strain maps E_{xx}, E_{yy} and E_{xy}, respectively, of the nanorod cross section. The black-white scale goes from -0.2 to 0.2.*

Neither of the images show clear indications of strain along any of the surfaces of the nanorod. A large defect in the nanorod (shown with an arrow in figure 5.7(a)) is clearly picked up in the strain maps, together with a dislocation extending from the defect to the edge of the nanorod. Other nanorod cross sections (not shown) have proven that also 90° domain walls can also be picked out, as has been shown earlier by Hÿtch *et al.* for bulk lead titanate [48].

A possible explanation of why the GPA images do not pick up any strain field is related to the quality of the specimen and the high resolution images. The nanorods have a lot of defects in them of various types and sizes, which all contribute to blur the high resolution images and introduce noise in the strain maps. This is visible already at the scale used in figure 5.7, and is even more pronounced if the absolute values of the maximum and minimum strain values are decreased.

5.4 Conclusions and outlook

The focus of this chapter has been somewhat different from the rest of this thesis, focusing on nanomaterials and more applied physics. The topic of nanostructured materials and nanostructured ferroelectrics in particular still has room for much exciting physics and many intriguing experiments, only some of which have been tested here. The ability to change the polarization direction is important for application purposes, and is easily confirmed even using conventional TEM methods. Further, the domain structure of such nanorods depends on a number of parameters and is in need of further both theoretical and experimental examination.

The usefulness of microtomy as a sample preparation technique to obtain a more thorough view of the structure of nanorods should not be underestimated, and the thorough characterization described in Paper 4 lays the basis for further studies of the nanorods.

While both holography and GPA are promising techniques for use on systems such as these ferroelectric nanorods, they are in the work described here hampered by defects and uneven imaging conditions in the nanorods. One can suspect that defects and voids in the nanorods are the reason why no phase contrast directly linked to the electric field was observed in the holograms, so that future attempts to do holography on ferroelectric nanorods should be done on samples with a less defected crystal structure.

The high resolution images used for GPA analysis are also affected by the presence of such defects, however the improved image quality in any defect free area or nanorod that could be obtained by aberration corrected high resolution imaging or even STEM (provided that suitable drift correction could be applied) would certainly constitute an advancement to the experiment as described here.

References

[1] Damjanovic D: *Ferroelectric, dielectric and piezoelectric properties of ferroelectric thin films and ceramics.* Rep. Prog. Phys. **61**, 1267 (1998).

[2] Setter N, Damjanovic D, Eng L *et al.*: *Ferroelectric thin films: Review of materials, properties, and applications.* J. Appl. Phys. **100**, 051606 (2006).

[3] Gregg JM: *Ferroelectrics at the nanoscale.* Phys. Status Solidi A **206**, 577 (2009).

[4] Ahn CH, Rabe KM and Triscone J-M: *Ferroelectricity at the nanoscale: Local polarization in oxide thin films and heterostructures.* Science **303**, 488 (2004).

[5] Zhong WL, Jiang B, Zhang PL *et al.*: *Phase-transition in* $PbTiO_3$ *ultrafine particles of different sizes.* J. Phys. Cond. Mater. **5**, 2619 (1993).

[6] Jiang B, Peng JL and Bursill LA: *Size effects on ferroelectricity of ultrafine particles of* $PbTiO_3$. J. Appl. Phys. **87**, 3462 (2000).

[7] Junquera J and Ghosez P: *Critical thickness for ferroelectricity in perovskite ultrathin films.* Nature **422**, 506 (2003).

[8] Schilling A, Adams TB, Bowman RM *et al.*: *Scaling of domain periodicity with thickness measured in BaTiO3 single crystal lamellae and comparison with other ferroics.* Phys. Rev. B **74**, 024115 (2006).

[9] Cohen RE: *Origin of ferroelectricity in perovskite oxides.* Nature **358**, 136 (1992).

[10] Kuroiwa Y, Aoyagi S,Sawada A *et al.*: *Evidence for Pb-O Covalency in Tetragonal* $PbTiO_3$. Phys. Rev. Lett. **87**, 217601 (2001).

[11] Wang YG, Dec J and Kleemann W: *Study on surface and domain structures of PbTiO3 crystals by atomic force microscopy.* J. Appl. Phys. **84**, 6795 (1998).

[12] Lehnen P, Dec J and Kleemann W: *Ferroelectric domain structures of PbTiO3 studied by scanning force microscopy.* J. Phys. D **33**, 1932 (2000).

[13] Loppacher C, Schlaphof F, Schneider S *et al.*: *Lamellar ferroelectric domains in PbTiO3 grains imaged and manipulated by AFM.* Surf. Sci. **532**, 483 (2003).

[14] Wang J, Sandu CS, Colla E *et al.*: *Ferroelectric domains and piezoelectricity in monocrystalline* $Pb(Zr,Ti)O_3$ *nanowires.* Appl. Phys. Lett. **90**, 133107 (2007).

[15] Schilling A, Bowman R M, Catalan G *et al.*: *Morphological control of polar orientation in single-crystal ferroelectric nanowires.* Nano Lett. **7**, 3787 (2007).

[16] Urban JJ, Spanier JE, Ouyang L *et al.*: *Single-crystalline barium titanate nanowires.* Adv. Mater. **15**, 423 (2003).

[17] Gu H, Hu Y, You J *et al.*: *Characterizaton of single-crystalline $PbTiO_3$ nanowire growth via surfactant-free hydrothermal method.* J. Appl. Phys. **101**, 024319 (2007).

[18] Lupascu DC: *Fatigue in ferroelectric ceramics and related issues.* Springer-Verlag, Berlin (2004).

[19] Lee J, Ramesh R, Keramidas VG *et al.*: *Imprint and oxygen deficiency in (Pb,La)(Zr,Ti)O_3 thin-film capacitors with La-Sr-Co-O electrodes.* Appl. Phys. Lett **66**, 1337 (1995).

[20] Sæterli R, van Helvoort ATJ, Wang G *et al.*: *Detailed TEM characterization of $PbTiO_3$ nanorods.* J. Phys.: Conf. Ser. **126**, 012010 (2008).

[21] Wang G, Sæterli R, Rørvik PM *et al.*: *Hierarchical nanostructures of $PbTiO_3$ through mesocrystal formation.* J. Nanosci. Nanotechn. **7**, 2538 (2007).

[22] Wang G, Sæterli R, Rørvik PM *et al.*: *Self-assembled growth of $PbTiO_3$ nanoparticles into microspheres and bur-like structures.* Chem. Mater. **19**, 2213 (2007).

[23] Lichte H, Formaned P, Lenk A *et al.*: *Electron Holography: Applications to materials questions.* Annu. Rev. Mater. Res. **37**, 539 (2007).

[24] Orchowski A, Rau WD, Lichte H *et al.*: *Electron holography surmounts resolution limit of electron-microscopy.* Phys. Rev. Lett. **74**, 399 (1995).

[25] Gabor D: *A new microscopic principle.* Nature **161**, 777 (1948).

[26] Simon P, Lichte H, Formanek P *et al.*: *Electron holography of biological samples.* Micron **39**, 229 (2008).

[27] Rau WD, Schwander P, Baumann FH *et al.*: *Two-Dimensional Mapping of the Electrostatic Potential in Transistors by Electron Holography.* Phys. Rev. Lett. **82**, 2614 (1999).

[28] Heumann M, Uhlig T and Zweck J: *True Single Domain and Configuration-Assisted Switching of Submicron Permalloy Dots Observed by Electron Holography.* Phys. Rev. Lett. **94**, 077202 (2005).

[29] Dunin-Borkowski RE, McCartney MR, Frankel RB *et al.*: *Magnetic microstructure of magnetotactic bacteria by electron holography.* Science **282**, 1868 (1998).

[30] Matsumoto T, Koguchi M, Suzuki K *et al.*: *Ferroelectric 90 degrees domain structure in a thin film of BaTiO*$_3$ *fine ceramics observed by 300 kV electron holography.* Appl. Phys. Lett. 92, 072902 (2008).

[31] Lichte H, Reibold M, Brand K and Lehmann M: *Ferroelectric electron holography.* Ultramicr. **93**, 199 (2002).

[32] Tonomura A: *Applications of electron holography.* Rev. Mod. Phys **59**, 639 (1987).

[33] Shirane G, Hoshino S and Suzuki K: *X-Ray Study of the Phase Transition in Lead Titanate.* Phys. Rev. **80**, 1105 (1950).

[34] Kalinicheva AG, Bass JD, Sun BN and Payne DA: *Elastic properties of tetragonal PbTiO*$_3$ *single crystals by Brillouin scattering.* J. Mater. Res. **12**, 2623 (1997).

[35] Liu J: *Scanning transmission electron microscopy and its application to the study of nanoparticles and nanoparticle systems.* Journal of Electron Microscopy **54**, 251 (2005).

[36] Pennycook SJ and Jesson DE: *High-resolution Z-contrast imaging of crystals.* Ultramicr. **37**, 14 (1991).

[37] Browning ND, Wallis DJ, Nellist PD *et al.*: *EELS in the STEM: Determination of materials properties on the atomic scale.* Micron **28**, 333 (2007).

[38] Batson PE: *Simultaneous STEM imaging and electron-energy-loss spectroscopy with atomic-column sensitivity.* Nature **366**, 727 (1993).

[39] Nellist PD and Pennycook SJ: *Incoherent imaging using dynamically scattered coherent electrons.* Ultramicr. **78**, 111 (1999).

[40] Humphreys CJ: *The scattering of fast electrons by crystals.* Rep. Prog. Phys **42**, 122 (1979).

[41] Williams DB and Carter CB: *Transmission Electron Microscopy.* Springer Science, New York (2009).

[42] Geuens P and van Dyck D: In *Advances in Imaging and Electron Physics Vol. 136.* Hawkes, PW (ed.) Elsevier Academic Press, San Diego (2005).

[43] Spence, JCH and Taftø, J: *Crystal site location of iron and trace elements in a magnesium-iron olivine by a new crystallographic technique.* Science **218**, 49 (1982).

[44] Tatsumi K, Muto S, Yamamoto Y *et al.*: *Site-specific electronic structure analysis by channeling EELS and first-principles calculations.* Ultramicr. **106**, 1019 (2006).

[45] Roussow CJ, Allen LJ, Findlay SD and Oxley MP: *Channeling effects in atomic resolution STEM.* Ultramicr. **96**, 299 (2003).

[46] Yu Z, Muller DA and Silcox J: *Study of strain fields at a-Si/ c-Si interface.* J. Appl. Phys. **95**, 3362 (2004).

[47] Fitting L, Thiel S, Schmehl A *et al.*: *Subtleties in ADF imaging and spatially resolved EELS: A case study of low-angle twist boundaries in* $SrTiO_3$. Ultramicr. **106**, 1053 (2006).

[48] Hÿtch MJ, Snoeck E and Kilaas R: *Quantitative measurement of displacement and strain fields from HREM micrographs.* Ultramicroscopy **74**, 131 (1998).

[49] Taraci JL, Hÿtch MJ, Clement T *et al.*: *Strain mapping in nanowires.* Nanotechnology **16**, 2365 (2005).

[50] Hüe F, Hÿtch MJ, Bender H *et al.*: *Direct mapping of strain in a strained-silicon transistor by high-resolution electron microscopy.* Phys. Rev. Lett. **100**, 156602 (2008).

Chapter 6

On the O K edge of $HoMnO_3$

This chapter deals with the hexagonal multiferroic holmium manganite, $HoMnO_3$, and its electronic structure. $HoMnO_3$ is ferroelectric at room temperature, and additionally antiferromagnetic at low temperatures [1]. Thus, while much attention has been given to the low-temperature multiferroic properties, the room - and high temperature properties are less understood. In the following chapter, I explore the possibility of utilizing EELS and ELNES to the study of room-temperature electronic properties of $HoMnO_3$. While this is by no means a finished piece of work, it lays the foundations of what may be an important contribution to the understanding of the electronic structure of $HoMnO_3$ and other hexagonal rare-earth manganites and is, as such, still worthy of a place in this thesis.

6.1 Introduction

$HoMnO_3$ is a rare-earth manganite with the same structure as the more studied $YMnO_3$. The rare earth manganites come in two crystallographic structures depending on the atomic radius of the rare earth ion [2]: The early rare earths up to Dy with large ionic radius crystallize in an orthorhombic space group, while the later rare earth compounds with smaller radii obtain the hexagonal variant[1].

This hexagonal crystal structure belongs to space group $P6_3cm$, and is characterized by two-dimensional layers of corner-sharing MnO_5 trigonal bipyramids. Ho ions reside in between the layers, as depicted in figure 6.1. Both Ho and Mn have nominally 3+ valences, and while Mn and O are covalently bound, the Ho atoms have ionic bonds to the rest of the structure [2]. Above T_c, the Ho atoms are found at the mirror plane between untilted bipyramids, while upon lowering the temperature through T_c, both the bipyramids and the layer of Ho atoms buckle to give rise to a net polarization. The Curie temperature of $HoMnO_3$ is about 600 °C (see e.g. [1] and references therein), and in addition it shows a polarization driven antiferromagnetic Mn^{3+} ordering up to about -160 °C [4].

The electronic structure of hexagonal $HoMnO_3$ has so far only been studied by theoretical means [2], concluding that there is a covalent bond between the Mn d and O p states, and that these states dominate the bottom of the lowest-lying conduction band.

---

[1] Although orthorhombic $HoMnO_3$ can be synthesized for example by the application of pressure [3].

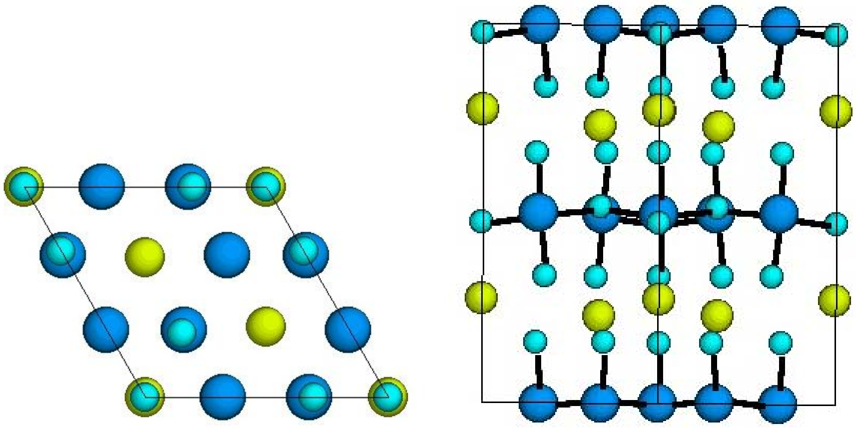
(a) (b)

Figure 6.1: *The unit cell of* $HoMnO_3$ *shown from (a) [001] and (b) [110] zone axis. Mn atoms are shown in blue, Ho atoms in yellow and O atoms in green. The Mn - O bonds in the* MnO_5 *bipyramids are outlined in black in (b) for clarity.*

6.2 Experimental details

The EELS experiments in this chapter have been performed on a JEOL 2010F in convergent beam mode with a Gatan imaging filter (GIF) attached. Both beam convergence angle and GIF acceptance angle are in the order of a few mrads, and a sum over several orientations is used in the presented spectrum. Each of the individual spectra has an energy resolution of about 1 eV, and was background subtracted and deconvoluted to obtain a single-scattering distribution. Sample thicknesses ranged from 0.2 to 0.5 t/λ.

No attempt to measure any chemical shift has been made, thus the exact energy loss of the peaks can vary with a few eV from the energy loss scale. However, the relative position of the peaks compared to the edge onset is correct.

The material was found to be beam sensitive, with large variations in the O K edge upon continued illumination (although no effect was visible in bright field TEM), see figure 6.2. Care was therefore taken to ensure pristine areas of examination and illumination times shorter than the time scale at which any visible effects to the spectrum set in.

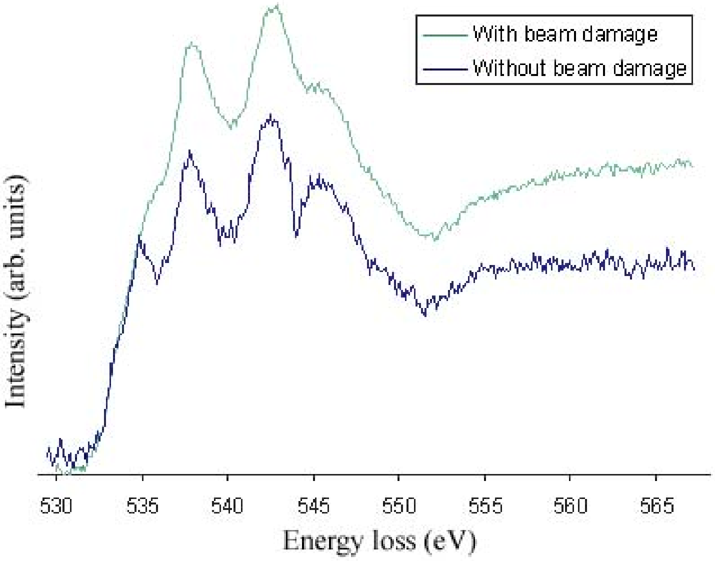

Figure 6.2: *Effect of beam damage on the O K edge of HoMnO$_3$. Notice the reduced intensity of the peaks at about 535 and 545 eV, and the increased separation of the peaks at about 537 and 542 eV.*

Unit cell parameters and atomic positions used in calculations were adopted from Muñoz *et al.* [5]. Lattice parameters of $a = 6.14$ and $c = 11.41$ were used, together with the atomic positions in Table 6.1. Prior to EELS experiments, selected area diffraction patterns were obtained from several orientations of the crystals in order to ensure the correct structure, see figure 6.3 for an example from the [110] zone axis.

Real-space multiple scattering calculations were performed on clusters consisting of about 170 atoms. Calculations were performed both with and without a core hole. Since there are four inequivalent O sites in hexagonal HoMnO$_3$, the O K edge of all four sites have been simulated and added according to the cite multiplicity (from table 6.1) for comparison to the experimental spectrum.

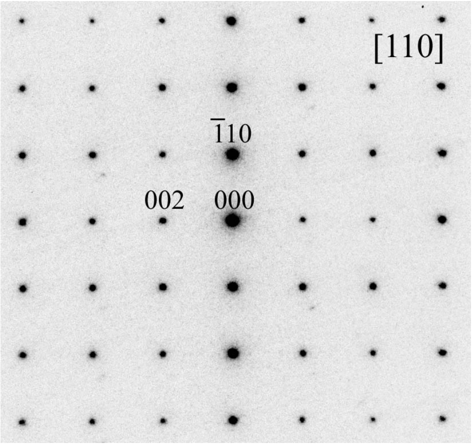

Figure 6.3: *Selected area diffraction pattern from [110] zone axis of* $HoMnO_3$.

Table 6.1: *Atomic positions of* $HoMnO_3$ *used in the RSMS calculations. From Muñoz* et al. *[5].*

Atom	**Site**	**x**	**y**	**z**
Ho	2a	0	0	0.273
Ho	4b	1/3	2/3	0.231
Mn	6c	0.322	0	0
O_I	6c	0.305	0	0.160
O_{II}	6c	0.643	0	0.333
O_{III}	4b	0	0	0.476
O_{IV}	2a	1/3	2/3	0.017

6.3 Results and discussion

Figure 6.4 shows the experimental O K edge of $HoMnO_3$, overlaid with RSMS simulations done through FEFF8. Both simulations with and without a core hole are shown, with a clearly better fit for the simulation including the core hole. Four distinct peaks labeled A-D can be discerned both in the near-edge structure and in the calculations, although the intensity of the first peak A is overestimated for both calculations.

Symmetry-projected DOS from RSMS calculations are shown in figure 6.5.

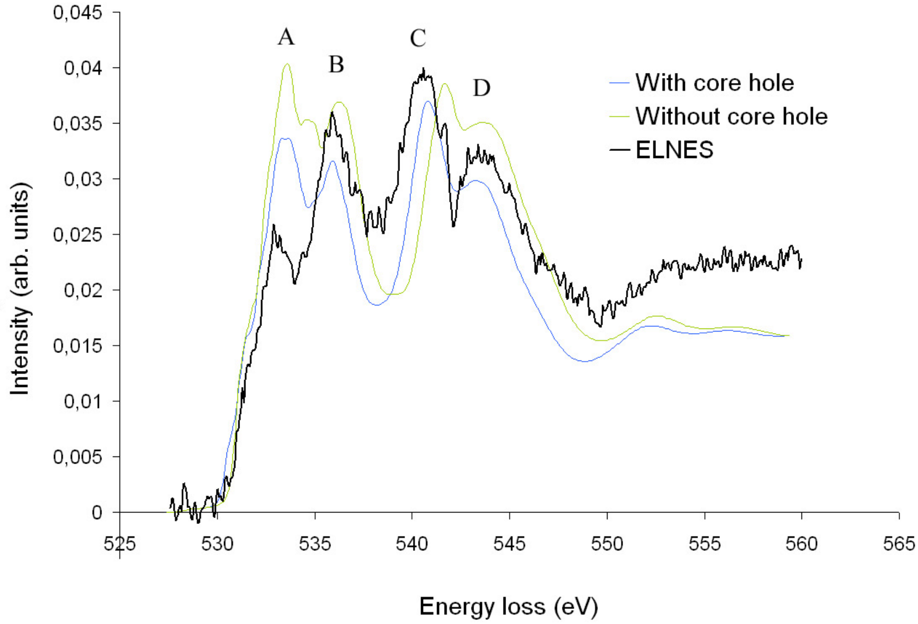

Figure 6.4: *Experimental ELNES (black) of the O K edge of HoMnO$_3$. Blue and green curves are near edge structures simulated with and without a core hole, respectively.*

They show that the edge shape is affected to a high degree of the excited properties of the O atom, particularly peak C has no clear analogue in the ground state DOS and seems to originate from an interaction of the excited O atom with Ho *d* states.

O *p* states are spread out across the conduction band, however Ho *f* states are sharply peaked at the low-energy side of the conduction band. Further up in energy, Mn d states dominate in the range 2-6 eV while Ho d states are found in the range 5-11 eV above the conduction band onset. The A and B peaks can be contributed to the covalent O - Mn band, however the overlap also of Ho *d* states at about 6 eV could in principle suggest that also Ho is involved in covalent bonding. The origin of peak D is less clear, but can possibly be attributed to O p - Mn p state covalent bonding.

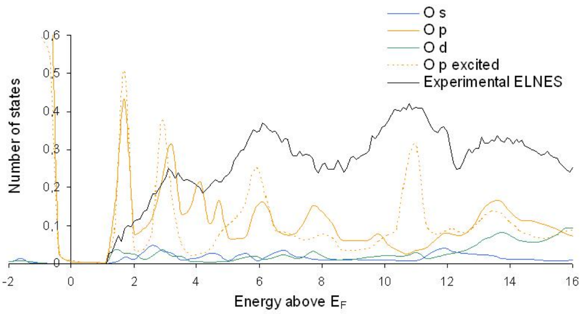

(a)

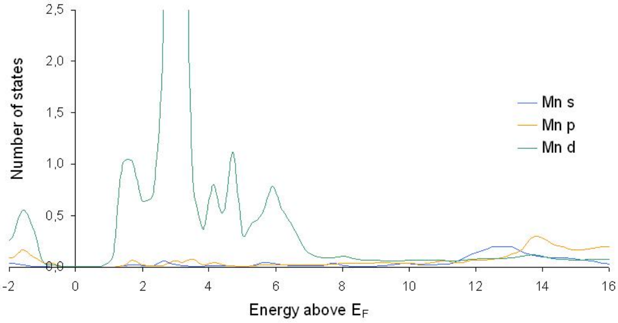

(b)

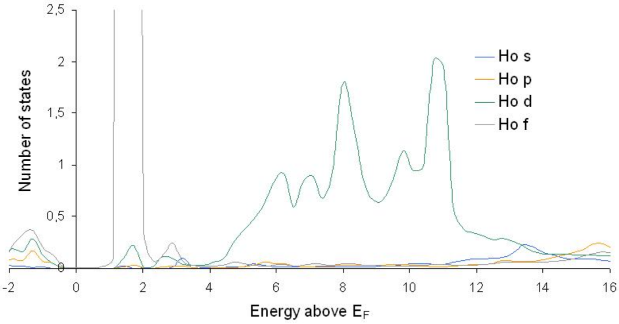

(c)

Figure 6.5: *Simulated density of states of HoMnO*$_3$*: (a) O states, (b) Mn states and (c) Ho states.* s *states are shown in blue,* p *states in orange,* d *states in green and* f *states in grey. Additionally, O* p *states of the excited atom are shown by an orange dashed line and the experimental O K edge (in arbitrary units) by a black line.*

6.4 Conclusions and outlook

These first attempts to study the O K edge of $HoMnO_3$ have provided an initial insight into the electronic structure. To proceed, more experiments could be conducted in which some parameters are changed, for example the study of the high-temperature paraelectric phase could yield insight into the different electronic structure of this phase. Also, in analogy to the work presented on $BiFeO_3$ (chapter 4), substitution on either Ho or Mn sites can be accomplished and would probably lead to new insights.

The Mn $L_{2,3}$ edge at ~630 eV constitutes another viewpoint accessible to ELNES studies, and has previously lead to advances in the study of other materials containing Mn [6, 7].

While these preliminary studies have been performed at an energy resolution of ~1 eV, any enhancement of this number is clearly beneficial for further energy-loss studies.

References

[1] Lottermoser T, Lonkal T, Amann U *et al.*: *Magnetic phase control by an electric field.* Nature **430**, 541 (2004).

[2] Ren C-Y: *Atomic, electronic, and ferroelectric properties of manganite* $RMnO_3$ *(R=Ho,Er,Tm,Lu) in hexagonal and orthorombic phases.* Phys. Rev. B **79**, 125113 (2009).

[3] Alonso JA, Martinez-Lope MJ, Casais MT and Fernandez-Diaz MT: *Evolution of the Jahn-Teller distortion of* MnO_6 *octahedra in* $RMnO_3$ *perovskites (R = Pr, Nd, Dy, Tb, Ho, Er, Y): A neutron diffraction study.* Inorg. Chem **39**, 917 (2000).

[4] Hur N, Jeong IK, Hundley MF *et al.*: *Giant magnetoelectric effect in multiferroic* $HoMnO_3$ *with a high ferroelectric transition temperature.* Phys. Rev. B **79**, 134120 (2009).

[5] Muñoz A, Alonso JA, Martinez-Lope JM *et al.*: *Evolution of the Magnetic Structure of Hexagonal* $HoMnO_3$ *from Neutron Powder Diffraction Data.* Chem. Mater. **13**, 1497 (2001).

[6] Garvie LAJ and Craven, AJ: *High-resolution parallel electro-energy-loss spectroscopy of Mn L(2,3)-edges in inorganic manganese.* Phys. Chem. Miner **21**, 191 (1994).

[7] Paterson JH and Krivanek OL: *ELNES of 3d transition metal oxides II. Variations with oxidation state and crystal structure.* Ultramicr. **32**, 319 (1990).

List of Figures